MOX-Report No. 78/2021

Partitioned and monolithic algorithms for the numerical solution of cardiac fluid-structure interaction

Bucelli, M.; Dede', L.; Quarteroni, A.; Vergara, C.

Partitioned and monolithic algorithms for the numerical solution of cardiac fluid-structure interaction

Michele Bucelli[1,*], Luca Dede'[1], Alfio Quarteroni[1,2], Christian Vergara[3]

[1] MOX, Dipartimento di Matematica, Politecnico di Milano, P.zza Leonardo da Vinci 32, 20133 Milan, Italy
[2] Mathematics Institute, EPFL, Av. Piccard, CH-1015 Lausanne, Switzerland (Professor Emeritus)
[3] LABS, Dipartimento di Chimica, Materiali e Ingegneria Chimica "Giulio Natta", Politecnico di Milano, P.zza Leonardo da Vinci 32, 20133 Milan, Italy

December 2, 2021

Abstract

We review and compare different fluid-structure interaction (FSI) numerical methods in the context of heart modeling, aiming at assessing their computational efficiency for cardiac numerical simulations and selecting the most appropriate method for heart FSI. Blood dynamics within the human heart is characterized by active muscular action, during both contraction and relaxation phases of the heartbeat. The efficient solution of the FSI problem in this context is challenging, due to the added-mass effect (caused by the comparable densities of fluid and solid, typical of biomechanics) and to the complexity, nonlinearity and anisotropy of cardiac consitutive laws. In this work, we review existing numerical coupling schemes for FSI in the two classes of strongly-coupled partitioned and monolithic schemes. The schemes are compared on numerical tests that mimic the flow regime characterizing the heartbeat in a human ventricle, during both systole and diastole. Active mechanics is treated in both the active stress and active strain frameworks. Computational costs suggest the use of a monolithic method. We employ it to simulate a full heartbeat of a human ventricle, showing how it allows to efficiently obtain physiologically meaningful results.

1 Introduction

The aim of this paper is to provide for the first time a systematic review and comparison of different fluid-structure interaction (FSI) numerical coupling schemes in the context of cardiac hemodynamics. In particular, we consider partitioned fully-coupled and monolithic algorithms and we analyze their effectiveness in both systolic and diastolic phases, and with both active stress and active strain modeling frameworks for muscular contraction. We investigate the performance of the schemes during the different phases of the heartbeat, in order to assess to which extent they depend on the specific physical features of such phases, in particular the presence of active forces.

The human heart acts as a pump, driven by the electrical activation of its cells, whose purpose is to force the blood into the circulatory system, allowing the delivery of oxygen and nutrients to the whole body [57]. The feedback mechanism between blood and cardiac muscle is relevant in determining the cardiac function and its response to pathological conditions [85, 86]. Numerical simulations offer a valid tool for the investigation of this mechanism [77].

A large number of computational studies model the fluid-solid feedback in the heart only in terms of a zero dimensional, lumped model for the blood flow [11, 19, 51, 58], mostly focusing on the electromechanical processes [11, 38, 48, 82, 83, 86]. Alternatively, three dimensional models for the blood flow

---

* Corresponding author
Email addresses: `michele.bucelli@polimi.it` (Michele Bucelli), `luca.dede@polimi.it` (Luca Dede'), `alfio.quarteroni@polimi.it` (Alfio Quarteroni) `christian.vergara@polimi.it` (Christian Vergara)

are one-way coupled to mechanical models, receiving as input results of mechanical simulations to prescribe the boundary displacement of the fluid domain, but without feedback from the three dimensional fluid model to the solid [56, 94, 103]. While FSI models for cardiac valves have been extensively studied [10, 27, 32, 50, 53, 63, 92], three dimensional fluid dynamics models of blood in the cardiac cavities are seldom two-ways coupled with mechanical models for the cardiac muscle [25, 65, 71, 87, 90, 98, 100], due to the inherent complexity and computational cost of FSI simulations.

In the context of biomechanics, solving FSI problems poses significant challenges on the stability and efficiency of the numerical solution, mainly because of the comparable densities of fluid and solid (resulting in the added mass effect [24]) and the anisotropy and nonlinearity of the constitutive laws [46, 52]. Appropriate schemes are required to enforce the fluid-solid coupling in a computationally efficient way.

The FSI numerical coupling schemes that have been proposed in the literature (see e.g. [26] for a review) can be roughly classified into partitioned loosely coupled (or explicit) schemes [16, 22, 23, 36, 45, 44, 47], partitioned fully coupled (or fixed-point, or implicit) schemes [13, 14, 24, 60, 61, 66, 68] and monolithic (or Newton-based) schemes [40, 71, 101]. The schemes differ significantly in their modularity and in the implementation effort that they require, and in terms of their performance [59, 61].

The effectiveness of FSI schemes in the context of vascular hemodynamics has been widely studied, e.g., in [13, 14, 59, 61]. However, the benchmarks and test cases under consideration were mostly related to the flow of blood within large vessels, rather than to the flow within cardiac chambers. In the heart, the flow is mostly driven by the interaction of the blood with the active muscular action (either contraction or relaxation, changing over time according to the heartbeat phase), and possibly with cardiac valves. The resulting flow is characterized by alternating systolic and diastolic phases. The former is characterized by fast dynamics, driven by the contraction of the muscle, with the flow featuring a transition regime towards turbulence [20, 96, 97, 102]. Diastole on the other hand is characterized by slower dynamics, and the flow is determined by the interplay between the ventricle relaxation and passive mechanical properties together with inflow conditions, resulting in a balloon-type problem [14]. Moreover, the material models required to describe effectively the muscular tissue are characterized by significant nonlinearity and anisotropy [46, 52]. All these aspects play a role in the effectiveness and efficiency of the schemes used for the solution of the FSI problem.

After introducing the mathematical models used, we review several existing FSI coupling schemes. We consider benchmark cases that mimic the characteristics of the human left ventricle, although in a simplified setting from the geometric viewpoint. Different tests allow us to separately analyze the systolic ejection and diastolic filling phases of the heartbeat. Concerning in particular the systolic phase, we employ both the active stress and active strain modeling frameworks for the active contraction of the cardiac muscle, and for both we compare the effectiveness of the coupling schemes. The computational times for the different methods indicate that, for all phases and with both activation models, a monolithic approach is more suited to the strong coupling of fluid and structure in the cardiac context. Finally, we present a numerical example simulating a full heartbeat, including isovolumetric phases.

The rest of the paper is organized as follows: Section 2 introduces the mathematical models that are used in the benchmark cases, and Section 3 briefly describes the temporal and spatial discretization schemes employed. Section 4 reviews the different coupling schemes under consideration. Section 5 discusses the numerical tests, and Section 6 draws some conclusive remarks.

2   Mathematical models for cardiac fluid-structure interaction

We consider a mechanical system defined in an open, bounded, time dependent domain $\Omega^t \subset \mathbb{R}^3$ (where $t \in [0, T)$ denotes the time variable). Such domain is decomposed into two subdomains Ω_f^t and Ω_s^t, the former occupied by a Newtonian, incompressible fluid, the latter occupied by a hyperelastic structure. We denote by $\Sigma^t = \partial \Omega_f^t \cap \partial \Omega_s^t$ the moving fluid structure interface, and by $\mathbf{n}$ the unit vector normal to Σ^t, outward directed from the fluid domain, inward directed into the structure domain.
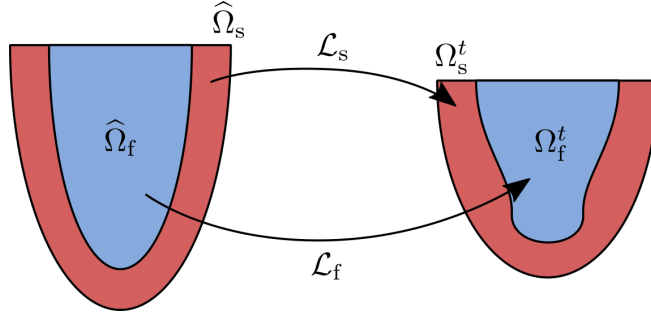
Figure 1: Schematic representation of the solid and fluid domains, in their reference (left) and current (right) configurations.

To track the motion over time of the subdomains, we introduce a fixed reference configuration, denoted by a hat (see Figure 1 for a schematic representation): $\widehat{\Omega}$, $\widehat{\Omega}_f$, $\widehat{\Omega}_s$, $\widehat{\Sigma}$ and $\widehat{\mathbf{n}}$ represent the reference configurations for the domain Ω, the fluid and solid domains, the fluid-solid interface and the normal unit vector respectively. We introduce the following maps from the reference to the time-dependent configurations:

$$\mathcal{L}_s : \widehat{\Omega}_s \times (0,T) \to \Omega_s^t \qquad \Omega_s^t = \{\mathbf{x} = \mathcal{L}_s(\widehat{\mathbf{x}},t) , \widehat{\mathbf{x}} \in \widehat{\Omega}_s\} ,$$
$$\mathcal{L}_f : \widehat{\Omega}_f \times (0,T) \to \Omega_f^t \qquad \Omega_f^t = \{\mathbf{x} = \mathcal{L}_f(\widehat{\mathbf{x}},t) , \widehat{\mathbf{x}} \in \widehat{\Omega}_f\} .$$

The evolution in time of the time-dependent domains is then expressed by the time-dependence of the maps $\mathcal{L}_s$ and $\mathcal{L}_f$. The precise definition of the maps is different for the fluid and the solid domains, and is detailed later.

In the following, we will refer to the time-dependent domains as the current configuration. We will denote by $\mathbf{x} \in \Omega^t$ spatial coordinates in the current configuration, and with $\widehat{\mathbf{x}} \in \widehat{\Omega}$ spatial coordinates in the reference configuration.

2.1 Structure problem

We model the structure as a hyperelastic material in the Lagrangian setting [72]. Let ρ_s be the density of the structure, and $\widehat{\mathbf{d}}(\widehat{\mathbf{x}},t)$ be its displacement at point $\widehat{\mathbf{x}}$ in the reference configuration and time t. Then, the map $\mathcal{L}_s$ from the reference to the current configuration is given by

$$\mathbf{x}(\widehat{\mathbf{x}},t) = \mathcal{L}_s(\widehat{\mathbf{x}},t) = \widehat{\mathbf{x}} + \widehat{\mathbf{d}}(\widehat{\mathbf{x}},t) \qquad \mathbf{x} \in \Omega_s, \widehat{\mathbf{x}} \in \widehat{\Omega}_s, t \in (0,T) .$$

We will denote by $F = I + \widehat{\nabla}\mathbf{d}$ the deformation gradient tensor, and with $J = \det F$ its determinant. The evolution of the structure displacement is described by the following partial differential equation (PDE), expressing the balance of momentum in the reference configuration [72]:

$$\rho_s \frac{\partial^2 \widehat{\mathbf{d}}}{\partial t^2} - \widehat{\nabla} \cdot P_s(\widehat{\mathbf{d}},t) = \mathbf{0} \qquad \text{in } \widehat{\Omega}_s \times (0,T) , \tag{1}$$

endowed with suitable initial conditions prescribing the displacement $\widehat{\mathbf{d}}$ and its temporal derivative at time $t = 0$ and boundary conditions on $\partial\widehat{\Omega}_s \backslash \widehat{\Sigma}$ (while on $\widehat{\Sigma}$ the FSI interface conditions are imposed, as described in Section 2.4). In (1), $P_s(\widehat{\mathbf{d}},t)$ is the first Piola-Kirchhoff stress tensor, defined as a function of the displacement $\widehat{\mathbf{d}}$ by the constitutive relation of the material. Since our aim is the mathematical modeling of cardiac mechanics, we incorporate active contraction in the stress tensor, either in the active stress [5, 71, 81, 87] or active strain [4, 40, 41, 84] framework.

We remark that in principle active contraction in either framework is generated by coupling the mechanical model with an electrophysiology model through an active force generation model, thus

resulting in an electromechanical model [12, 41, 48, 78, 77, 81, 84, 87]. Since our focus is on the FSI numerical schemes, we prescribe the evolution of active stress or strain using an analytical law (hence the explicit dependence of P_s on the time t). In what follows, we address two models considered in the literature for the active contraction, together with the passive model.

2.1.1 Active mechanics: active stress formulation

Within the active stress framework, the tensor P_s is decomposed as the sum of a passive and an active part: $P_s = P_{\text{pas}} + P_{\text{act}}$. The passive part is defined as the derivative of a suitable strain energy function $\mathcal{W}(F)$:

$$P_{\text{pas}} = \frac{\partial \mathcal{W}}{\partial F} \ ,$$

wherein $\mathcal{W}$ characterizes the passive properties of the material.

Let us introduce at each point of $\widehat{\Omega}_s$ a unit vector $\mathbf{f}$ that describes the local direction of the muscular fibers along which active force is generated [74]. The active part of the stress tensor is defined as

$$P_{\text{act}} = T_{\text{act}} \frac{F\mathbf{f} \otimes \mathbf{f}}{\sqrt{I_{4f}}} \ ,$$

where T_{act} is an active tension in the direction of fibers [5, 81, 87]. As stated before, T_{act} is not derived by the coupling with an electrophysiology model, rather, it is analytically prescribed.

2.1.2 Active mechanics: active strain formulation

In the active strain framework, the deformation gradient is assumed to be decomposed multiplicatively as $F = F_{\text{pas}}F_{\text{act}}$. F_{act} is the gradient of a deformation from the reference configuration to a virtual intermediate configuration only determined by the active contraction, and F_{pas} is the gradient of a deformation from this virtual configuration to the current configuration, due to the passive mechanical behavior of the material [5]. The stress tensor is defined as the derivative of the strain energy function with respect to the deformation gradient tensor. The strain energy function is expressed as function of the passive deformation gradient only, i.e.

$$P_s = \frac{\partial \mathcal{W}(F_{\text{pas}})}{\partial F} \ .$$

The active deformation gradient is defined as

$$F_{\text{act}} = I + \gamma_{\text{f}} \mathbf{f} \otimes \mathbf{f} \ ,$$

where γ_{f} is the strain in the direction of fibers [5, 41, 40, 84]. For γ_{f}, the same comments of above regarding T_{act} hold true.

2.1.3 Passive mechanics: constitutive model

We consider the Guccione constitutive model [46, 82, 95], commonly used for cardiac tissue. We introduce at each point of $\widehat{\Omega}_s$ a reference system $\{\mathbf{f}, \mathbf{s}, \mathbf{n}\}$ describing the direction of fibers, sheetlets and cross-fibers respectively [74]. Then, the strain energy function is given by:

$$\mathcal{W} = \frac{c}{2}\left(e^{Q(F)} - 1\right) + \frac{k}{2}(J-1)\log(J) \ , \tag{2}$$
$$Q(F) = \sum_{\mathbf{i,j}\in\{\mathbf{f,s,n}\}} a_{\mathbf{i,j}}(E\mathbf{i}\cdot\mathbf{j}) \ ,$$
$$E = \frac{1}{2}\left(F^T F - I\right) \ ,$$

4

where c and $a_{\mathbf{i},\mathbf{j}}$, $\mathbf{i},\mathbf{j} \in \{\mathbf{f},\mathbf{s},\mathbf{n}\}$ are positive parameters and k is the bulk modulus.

We incorporate the quasi-incompressibility of the material by adding the term $\dfrac{k}{2}(J-1)\log(J)$ in the strain energy function that penalizes volume variations (i.e. penalizes values of J that are away from 1) [80, 95].

For ventricular test cases, the reference system $\{\mathbf{f},\mathbf{s},\mathbf{n}\}$ is generated by means of the rule-based method proposed by Rossi et al. [84].

2.2 Displacement of the fluid domain

We model the fluid dynamics in a moving domain in the ALE framework [55, 88]. The structure displacement at the fluid-structure interface is extended to the fluid domain by solving the following harmonic extension problem: for every $t \in (0,T)$,

$$\begin{cases} -\widehat{\Delta}\widehat{\mathbf{d}}_{\mathrm{f}} = \mathbf{0} & \text{in } \widehat{\Omega}_{\mathrm{f}}, \\ \widehat{\mathbf{d}}_{\mathrm{f}} = \mathbf{0} & \text{on } \widehat{\Gamma}_{\mathrm{f}}^{\mathrm{D}}, \\ (\widehat{\nabla}\widehat{\mathbf{d}}_{\mathrm{f}})\widehat{\mathbf{n}} = \mathbf{0} & \text{on } \widehat{\Gamma}_{\mathrm{f}}^{\mathrm{N}}, \end{cases} \tag{3}$$

where $\widehat{\Gamma}_{\mathrm{f}}^{\mathrm{D}}$ and $\widehat{\Gamma}_{\mathrm{f}}^{\mathrm{N}}$ are subsets of $\partial\widehat{\Omega}_{\mathrm{f}}\backslash\widehat{\Sigma}$ on which Dirichlet and Neumann conditions, respectively, are prescribed. On $\widehat{\Sigma}$, interface conditions are prescribed as detailed in Section 2.4. The map $\mathcal{L}_{\mathrm{f}}$ from the reference to the current configuration of the fluid domain is given by

$$\mathbf{x} = \widehat{\mathbf{x}} + \widehat{\mathbf{d}}_{\mathrm{f}}(\widehat{\mathbf{x}},t) \qquad \mathbf{x} \in \Omega_{\mathrm{f}}, \ \widehat{\mathbf{x}} \in \widehat{\Omega}_{\mathrm{f}}, \ t \in (0,T) \ .$$

We define the fluid domain velocity $\mathbf{u}_{\mathrm{f}}$ as the time derivative of the fluid domain displacement, i.e.

$$\widehat{\mathbf{u}}_{\mathrm{f}} = \frac{\partial\widehat{\mathbf{d}}_{\mathrm{f}}}{\partial t} \qquad \text{in } \widehat{\Omega}_{\mathrm{f}} \ .$$

Then, we map it onto the current configuration through $\mathcal{L}_{\mathrm{f}}$:

$$\mathbf{u}_{\mathrm{f}} = \widehat{\mathbf{u}}_{\mathrm{f}}(\mathcal{L}_{\mathrm{f}}^{-1}(\mathbf{x},t),t) \ .$$

We remark that the extension of the displacement from the interface to the fluid domain is arbitrary, and other differential operators (other than the laplacian) can be considered. In particular, a linear elasticity lifting operator can be employed to this aim [88].

2.3 Fluid dynamics problem

We model the blood as a Newtonian incompressible fluid. Denoting by ρ_{f} the fluid density and by $\mathbf{u}$ and p its velocity and pressure, respectively, the balance of momentum and mass conservation equations are expressed by the Navier-Stokes equations in ALE coordinates [76]:

$$\begin{cases} \rho_{\mathrm{f}}\left[\dfrac{\partial\mathbf{u}}{\partial t} + ((\mathbf{u} - \mathbf{u}_{\mathrm{f}}) \cdot \nabla)\,\mathbf{u}\right] - \nabla \cdot \sigma_{\mathrm{f}}(\mathbf{u},p) = \mathbf{0} & \text{in } \Omega_{\mathrm{f}}^{t} \times (0,T) \ , \\ \nabla \cdot \mathbf{u} = 0 & \text{in } \Omega_{\mathrm{f}}^{t} \times (0,T) \ , \end{cases}$$

endowed with initial conditions ($\mathbf{u}$ in Ω_{f}^{0}), and suitable boundary conditions on $\partial\Omega_{\mathrm{f}}^{t}\backslash\Sigma^{t}$ (while FSI interface conditions are imposed on Σ^{t}, see Section 2.4). The Cauchy stress tensor $\sigma_{\mathrm{f}}(\mathbf{u},p)$ is defined as

$$\sigma_{\mathrm{f}}(\mathbf{u},p) = 2\,\mu\,\varepsilon(\mathbf{u}) - p\,I \ , \qquad \varepsilon(\mathbf{u}) = \frac{1}{2}\left(\nabla\mathbf{u} + \nabla\mathbf{u}^{T}\right) \ ,$$

wherein μ is the dynamic viscosity of the fluid.

2.4 Fluid-structure coupling

A *geometric coupling* condition is imposed to enforce the continuity of displacements at the fluid-structure interface: $\widehat{\mathbf{d}}_{\mathrm{f}} = \widehat{\mathbf{d}}$ on $\widehat{\Sigma}$. Besides, two other coupling conditions are needed. The velocity at the fluid-structure interface must be continuous, i.e. $\mathbf{u} = \dfrac{\partial \mathbf{d}}{\partial t}$ on Σ; this corresponds to prescribing a no-slip condition on the fluid-structure interface, and is referred to as *kinematic coupling*. Moreover, the traction at the fluid-structure interface must be continuous, i.e. $\sigma_{\mathrm{f}}(\mathbf{u}, p)\mathbf{n} = \sigma_{\mathrm{s}}(\mathbf{d})\mathbf{n}$ on Σ^t, where $\sigma_{\mathrm{s}}(\mathbf{d}) = J^{-1} F P_{\mathrm{s}}(\mathbf{d})^T$ is the Cauchy stress tensor for the structure; this condition expresses Newton's third law across the fluid-structure interface, and is referred to as *dynamic coupling*.

The fully coupled FSI problem reads: find $\widehat{\mathbf{d}}, \widehat{\mathbf{d}}_{\mathrm{f}}, \mathbf{u}, p$ such that

$$
\begin{cases}
\rho_{\mathrm{s}} \dfrac{\partial^2 \widehat{\mathbf{d}}}{\partial t^2} - \widehat{\nabla}{\cdot}P_{\mathrm{s}}(\widehat{\mathbf{d}}, t) = \mathbf{0} & \text{in } \widehat{\Omega}_{\mathrm{s}} \times (0, T) , \\[2mm]
-\widehat{\Delta}\widehat{\mathbf{d}}_{\mathrm{f}} = \mathbf{0} & \text{in } \widehat{\Omega}_{\mathrm{f}} \times (0, T) , \\[2mm]
\widehat{\mathbf{d}}_{\mathrm{f}} = \widehat{\mathbf{d}} & \text{on } \widehat{\Sigma} \times (0, T) , \\[2mm]
(\widehat{\nabla}\widehat{\mathbf{d}}_{\mathrm{f}})\widehat{\mathbf{n}} = \mathbf{0} & \text{on } \partial\widehat{\Omega}_{\mathrm{f}}\backslash\widehat{\Sigma} \times (0, T) , \\[2mm]
\rho_{\mathrm{f}} \left[\dfrac{\partial \mathbf{u}}{\partial t} + ((\mathbf{u} - \mathbf{u}_{\mathrm{f}}) \cdot \nabla) \mathbf{u} \right] - \nabla \cdot \sigma_{\mathrm{f}}(\mathbf{u}, p) = \mathbf{0} & \text{in } \Omega_{\mathrm{f}}^t \times (0, T) , \\[2mm]
\nabla \cdot \mathbf{u} = 0 & \text{in } \Omega_{\mathrm{f}}^t \times (0, T) , \\[2mm]
\mathbf{u} = \dfrac{\partial \mathbf{d}}{\partial t} & \text{on } \Sigma \times (0, T) , \\[2mm]
\sigma_{\mathrm{f}}(\mathbf{u}, p)\mathbf{n} = \sigma_{\mathrm{s}}(\mathbf{d})\mathbf{n} & \text{on } \Sigma \times (0, T) ,
\end{cases}
\tag{4}
$$

endowed with suitable initial and boundary conditions for both the fluid and the solid.

To keep the notation light, we shall drop henceforth the hat over $\widehat{\mathbf{d}}$ and $\widehat{\mathbf{d}}_{\mathrm{f}}$. The context will make clear whether we are considering quantities in reference or current configuration.

3 Time and space discretizations

We use finite differences for the time discretization of the FSI problem (4) [76]. Let us introduce a partition of the time domain $(0, T)$ into N_t intervals of width Δt of extremes $t^0 = 0$, t^1, ..., $t^{N_t} = T$. In the following, we will denote by a superscript on a solution variable (including the domain Ω_{f} and the interface Σ) the time-discrete approximation of that variable at that timestep (e.g. $\mathbf{u}^n \approx \mathbf{u}(t = t^n)$). For the Navier-Stokes momentum equation, we use the implicit Euler scheme together with a semi-implicit discretization of the advection term [76]. For the structure problem, we use a first order backward finite difference scheme. For every $n = 0, 1, \ldots, N_t - 1$, and assuming $\mathbf{d}^{-1} = \mathbf{d}^0$, the

time-discrete problem reads:

$$
\begin{cases}
\rho_\mathrm{s} \dfrac{\mathbf{d}^{n+1} - 2\mathbf{d}^n + \mathbf{d}^{n-1}}{\Delta t^2} - \widehat{\nabla} \cdot P_\mathrm{s}(\mathbf{d}^{n+1}) = \mathbf{0} & \text{in } \widehat{\Omega}_\mathrm{s}, & \text{(5a)} \\[2ex]
-\widehat{\Delta} \mathbf{d}_\mathrm{f}^{n+1} = \mathbf{0} & \text{in } \widehat{\Omega}_\mathrm{f}, & \text{(5b)} \\[1ex]
\mathbf{d}_\mathrm{f}^{n+1} = \mathbf{d}^{n+1} & \text{on } \widehat{\Sigma}, & \text{(5c)} \\[1ex]
\mathbf{d}_\mathrm{f}^{n+1} = \mathbf{0} & \text{on } \widehat{\Gamma}_\mathrm{f}^\mathrm{D}, & \text{(5d)} \\[1ex]
(\widehat{\nabla} \mathbf{d}_\mathrm{f}^{n+1})\widehat{\mathbf{n}} = \mathbf{0} & \text{on } \widehat{\Gamma}_\mathrm{f}^\mathrm{N}, & \text{(5e)} \\[1ex]
\mathbf{u}_\mathrm{f}^{n+1} = \dfrac{\mathbf{d}_\mathrm{f}^{n+1} - \mathbf{d}_\mathrm{f}^n}{\Delta t} & \text{in } \widehat{\Omega}_\mathrm{f}, & \text{(5f)} \\[2ex]
\rho_\mathrm{f} \left[\dfrac{\mathbf{u}^{n+1} - \mathbf{u}^n}{\Delta t} + \left((\mathbf{u}^n - \mathbf{u}_\mathrm{f}^{n+1}) \cdot \nabla \right) \mathbf{u}^{n+1} \right] - \nabla \cdot \sigma_\mathrm{f}(\mathbf{u}^{n+1}, p^{n+1}) = \mathbf{0} & \text{in } \Omega_\mathrm{f}^{n+1}, & \text{(5g)} \\[2ex]
\nabla \cdot \mathbf{u}^{n+1} = 0 & \text{in } \Omega_\mathrm{f}^{n+1}, & \text{(5h)} \\[1ex]
\mathbf{u}^{n+1} = \dfrac{\mathbf{d}^{n+1} - \mathbf{d}^n}{\Delta t} & \text{on } \Sigma^{n+1}, & \text{(5i)} \\[2ex]
\sigma_\mathrm{f}(\mathbf{u}^{n+1}, p^{n+1})\mathbf{n} = \sigma_\mathrm{s}(\mathbf{d}^{n+1})\mathbf{n} & \text{on } \Sigma^{n+1}. & \text{(5j)}
\end{cases}
$$

Space discretization is obtained by means of the finite element method [54, 76], using hexahedral elements for both the fluid and the structure subdomains. We choose conforming meshes at the fluid and structure interface. We use SUPG-PSPG stabilization [28, 76, 93, 102] for the Navier-Stokes equations, enabling the use of trilinear polynomials ($\mathbb{Q}_1$) for both fluid velocity and pressure, and the stabilization of the advection dominated regime. We use $\mathbb{Q}_1$ polynomials also for the structure displacement and for the fluid domain displacement.

After space and time discretization, the FSI problem is expressed as a system of nonlinear algebraic equations: for each $n = 0, 1, \ldots, N_t - 1$,

$$
\begin{cases}
\mathbb{G}_\mathrm{f}(\mathbf{G}^{n+1}) = \mathbf{0}, \\
\mathbb{S}_\mathrm{s}(\mathbf{D}^{n+1}) = \mathbf{0}, \\
\mathbb{F}_\mathrm{f}(\mathbf{U}^{n+1}, \mathbf{G}^{n+1}) = \mathbf{0}, \\
\mathbb{C}_\mathrm{g}(\mathbf{G}^{n+1}, \mathbf{D}^{n+1}) = \mathbf{0}, \\
\mathbb{C}_\mathrm{k}(\mathbf{U}^{n+1}, \mathbf{D}^{n+1}) = \mathbf{0}, \\
\mathbb{C}_\mathrm{d}(\mathbf{D}^{n+1}, \mathbf{U}^{n+1}, \mathbf{G}^{n+1}) = \mathbf{0}.
\end{cases}
\tag{6}
$$

In the former system, the vectors $\mathbf{G}$, $\mathbf{D}$ and $\mathbf{U}$ denote the algebraic numerical representations of the fluid domain displacement $\mathbf{d}_\mathrm{f}$, structure displacement $\mathbf{d}$ and fluid domain variables (i.e. degrees of freedom associated to the velocity $\mathbf{u}$ and pressure p, collected in a single vector), respectively. The operators $\mathbb{G}_\mathrm{f}$, $\mathbb{S}_\mathrm{s}$ and $\mathbb{F}_\mathrm{f}$ are the algebraic numerical representations of the differential operators defining the fluid domain displacement problem (5b), the structure problem (5a) and the fluid problem (5g) and (5h), each of them restricted to the degrees of freedom on the interior (not on the interface) of the respective subdomains. To keep our notation light, the dependence of the operators on solution variables at timesteps until t^n is understood. The operators $\mathbb{C}_\mathrm{g}$, $\mathbb{C}_\mathrm{k}$ and $\mathbb{C}_\mathrm{d}$, are the algebraic numerical representations of the geometric (5c), kinematic (5i) and dynamic (5j) coupling conditions respectively. The explicit definition of each operator is given in Appendix A.

We remark that $\mathbb{G}_\mathrm{f}$, $\mathbb{C}_\mathrm{g}$ and $\mathbb{C}_\mathrm{k}$ are affine, whereas the remaining operators are in general nonlinear. In particular, we remark that the dependence of $\mathbb{F}_\mathrm{f}$ on $\mathbf{G}^{n+1}$ also accounts for the fact that the integrals involved in the weak formulation of the fluid problem are calculated on the deformed configuration (at time t^{n+1}) of the fluid domain.

4 Fluid-structure coupling schemes

The FSI problem is highly nonlinear, due to the nonlinearity of the fluid and structure problems (especially the latter) taken individually, and to the inherently nonlinear dependency of the fluid problem on the structure displacement through the fluid domain displacement. Suitable schemes need to be implemented to deal with the three subproblems (geometry, fluid, structure) and their coupling conditions.

In the context of biological tissues, the fluid and the structure have comparable densities, resulting in the so-called added-mass effect [24]. This typically yields stability issues: in particular, loosely coupled partitioned schemes (based on explicit time discretization of the whole FSI problem) may generate blowing-up solutions due to an incorrect energy balance [24]. Although in recent years stable loosely coupled partitioned schemes for hemodynamics were studied [16, 22, 23, 36, 45, 44, 47], here we focus on the two most traditional families of schemes that guarantee stability in hemodynamics:

- the *fully coupled partitioned schemes* [13, 14, 24, 26, 60, 66, 68, 87], in which at every timestep the fluid and structure subproblems are solved one independently of the other, applying suitable interface transmission conditions to each subproblem and iterating until fulfillment of the interface conditions (in the spirit of fixed-point iteration algorithms); for the sake of brevity we will refer to these schemes as partitioned, leaving it understood that we refer to fully coupled partitioned schemes;

- the *monolithic schemes* [18, 26, 40, 62, 70, 71, 101], in which the nonlinear algebraic system arising from the discretization of the FSI problem is solved as a whole by means of Newton or inexact-Newton schemes.

In both the cases, the geometric coupling can be treated either implicitly or explicitly without hindering the time stability of the numerical scheme [68]. The explicit treatment of the geometric coupling, together with the explicit treatment of the advection term in Navier-Stokes equations, gives rise to schemes referred to as geometric-convective explicit [15, 26, 34, 67, 69].

We remark that the classes above are not exhaustive: alternative approaches involve the use of splitting schemes [34, 75] or the reduction of the FSI problem to an interface problem [29].

In the following sections, several schemes within the partitioned and monolithic families are described. In each case we will consider the fully discrete problem (6), and use the notation introduced in Section 3.

4.1 Partitioned (P) schemes

The appeal of partitioned schemes lies in their modularity, i.e. in the fact that they reduce to a sequence of independent calls to fluid dynamics and mechanics solvers. Therefore, one can leverage available solvers and advanced techniques for the individual subproblems, provided there exists a way to communicate interface data between them. On the other hand, these are iterative schemes, whose convergence properties are difficult to assess in the most general case, and depend heavily on the material properties and geometry of the domain [13, 24, 39].

4.1.1 Partitioned schemes with explicit geometric coupling (PE)

A fixed-point, partitioned scheme with explicit geometric coupling can be outlined as follows: for each time step $n = 1, 2, \ldots, N_t$, given $\mathbf{G}^n$, $\mathbf{D}^n$ and $\mathbf{U}^n$, to obtain $\mathbf{G}^{n+1}$, $\mathbf{D}^{n+1}$ and $\mathbf{U}^{n+1}$:

1. compute $\mathbf{G}^{n+1}$ by solving the fluid domain displacement problem, using the structure displacement at previous time step:

$$\begin{cases} \mathbb{G}_{\mathrm{f}}(\mathbf{G}^{n+1}) = \mathbf{0} \,, \\ \mathbb{C}_{\mathrm{g}}(\mathbf{G}^{n+1}, \mathbf{D}^n) = \mathbf{0} \,, \end{cases}$$

and update the fluid domain according to the newly computed fluid domain displacement;
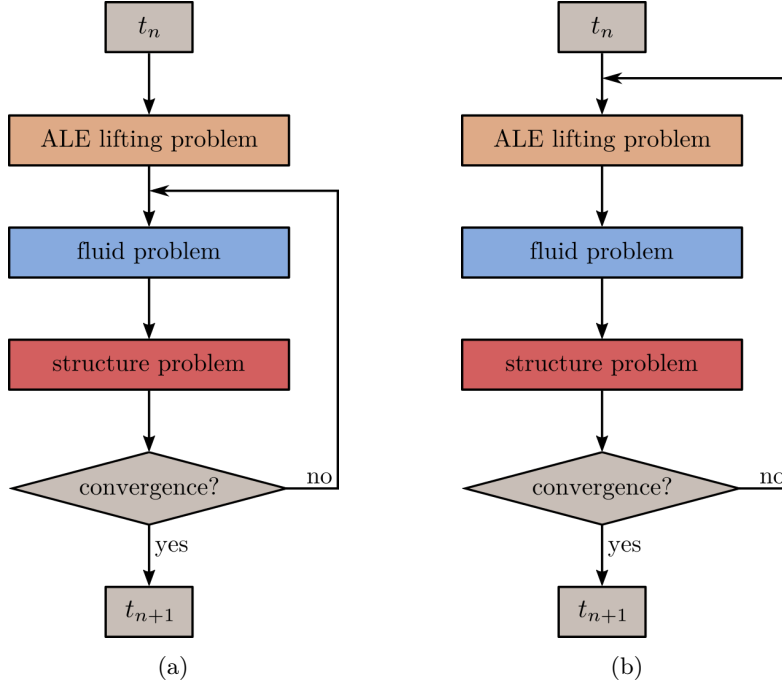
Figure 2: Partitioned schemes, with explicit geometric coupling (a) and implicit geometric coupling (b): advancement from one timestep to the following one is performed by iterating over the subproblems until convergence.

2. set $\mathbf{D}^{n+1}_{(0)} = \mathbf{D}^n$ and iterate for $k = 0, 1, 2, \ldots$ and until convergence:

   (a) compute $\mathbf{U}^{n+1}_{(k+1)}$ by solving the fluid problem, using the structure displacement and traction at previous iteration to provide suitable boundary data at the interface:

   $$\begin{cases} \mathbb{F}_f(\mathbf{U}^{n+1}_{(k+1)}, \mathbf{G}^{n+1}) = \mathbf{0} \,, \\ \mathbb{C}_f(\mathbf{D}^{n+1}_{(k)}, \mathbf{U}^{n+1}_{(k+1)}, \mathbf{G}^{n+1}) = \mathbf{0} \, ; \end{cases}$$

   (b) compute $\widetilde{\mathbf{D}}^{n+1}_{(k+1)}$ by solving the mechanics problem, using the just computed fluid domain solution to provide suitable boundary data at the interface:

   $$\begin{cases} \mathbb{S}_s(\widetilde{\mathbf{D}}^{n+1}_{(k+1)}) = \mathbf{0} \,, \\ \mathbb{C}_s(\widetilde{\mathbf{D}}^{n+1}_{(k+1)}, \mathbf{U}^{n+1}_{(k+1)}, \mathbf{G}^{n+1}) = \mathbf{0} \, ; \end{cases}$$

   (c) apply relaxation or acceleration to the structure displacement, by setting

   $$\mathbf{D}^{n+1}_{(k+1)} = \mathbb{R}_{(k+1)}(\widetilde{\mathbf{D}}^{n+1}_{(k+1)}, \mathbf{D}^{n+1}_{(k)}, \mathbf{D}^{n+1}_{(k-1)}, \ldots) \,,$$

   where $\mathbb{R}_{(k+1)}$ is a suitable relaxation or convergence acceleration operator, which can be either a relaxation with constant coefficient, Aitken acceleration or Anderson acceleration; more details are given in Appendix B.

Iterations are stopped when the norm of the residual associated to interface conditions falls below a prescribed tolerance, as described in [13].

9

The scheme is depicted in Figure 2a. The operators $\mathbb{C}_f$ and $\mathbb{C}_s$ represent suitable boundary conditions at the interface for each problem. Different algorithms are obtained by different choices of such operators. Two relevant options are the following:

- Dirichlet-Neumann (DN) scheme [13, 24]:

$$\mathbb{C}_f(\mathbf{D}_{(k)}^{n+1}, \mathbf{U}_{(k+1)}^{n+1}, \mathbf{G}^{n+1}) = \mathbb{C}_k(\mathbf{U}_{(k+1)}^{n+1}, \mathbf{D}_{(k)}^{n+1}) \,,$$
$$\mathbb{C}_s(\widetilde{\mathbf{D}}_{(k+1)}^{n+1}, \mathbf{U}_{(k+1)}^{n+1}, \mathbf{G}^{n+1}) = \mathbb{C}_d(\widetilde{\mathbf{D}}_{(k+1)}^{n+1}, \mathbf{U}_{(k+1)}^{n+1}, \mathbf{G}^{n+1}) \,,$$

  resulting in the kinematic coupling condition being applied to the fluid and the dynamic coupling condition being applied to the structure;

- Robin-Neumann (RN) scheme [13, 14]:

$$\mathbb{C}_f(\mathbf{D}_{(k)}^{n+1}, \mathbf{U}_{(k+1)}^{n+1}, \mathbf{G}^{n+1}) = \alpha_f \mathbb{C}_k(\mathbf{U}_{(k+1)}^{n+1}, \mathbf{D}_{(k)}^{n+1}) + \mathbb{C}_d(\mathbf{D}_{(k)}^{n+1}, \mathbf{U}_{(k+1)}^{n+1}, \mathbf{G}^{n+1}) \,,$$
$$\mathbb{C}_s(\widetilde{\mathbf{D}}_{(k+1)}^{n+1}, \mathbf{U}_{(k+1)}^{n+1}, \mathbf{G}^{n+1}) = \mathbb{C}_d(\widetilde{\mathbf{D}}_{(k+1)}^{n+1}, \mathbf{U}_{(k+1)}^{n+1}, \mathbf{G}^{n+1}) \,,$$

  where $\alpha_f > 0$ is a suitable parameter chosen to improve convergence [39].

Other schemes can be obtained in a similar way (e.g. Robin-Robin schemes, [9, 13, 14, 43]), by combining the kinematic and dynamic coupling conditions. We mainly consider these two because on the one hand the DN scheme is extremely simple to formulate and implement, on the other hand the RN scheme has been shown to perform particularly well in comparison to other fixed-point schemes, most notably DN [13, 14]. In any case, such schemes guarantee the fulfillment, up to a prescribed tolerance, of the kinematic and dynamic conditions.

We remark that the structure subproblem is in general nonlinear, and it must be solved e.g. by means of Newton's method at each iteration [76].

4.1.2 Partitioned schemes with implicit geometric coupling (PI)

A fixed-point scheme with implicit geometric coupling can be obtained by by iterating also over the geometric interface condition, solving (3) within the same loop used to achieve the convergence of both the kinematic and dynamic conditions. For each $n = 1, 2, \ldots, N_t$, given $\mathbf{G}^n$, $\mathbf{D}^n$ and $\mathbf{U}^n$, in order to compute $\mathbf{G}^{n+1}$, $\mathbf{D}^{n+1}$ and $\mathbf{U}^{n+1}$, we set $\mathbf{D}_{(0)}^{n+1} = \mathbf{D}^n$, and iterate for $k = 0, 1, 2, \ldots$ until convergence:

1. compute $\mathbf{G}_{(k+1)}^{n+1}$ by solving the fluid domain displacement problem, using the structure displacement at previous iteration:
$$\begin{cases} \mathbb{G}_f(\mathbf{G}_{(k+1)}^{n+1}) = \mathbf{0} \,, \\ \mathbb{C}_g(\mathbf{G}_{(k+1)}^{n+1}, \mathbf{D}_{(k)}^{n+1}) = \mathbf{0} \,, \end{cases}$$
   and update the fluid domain according to the newly computed fluid domain displacement;

2. compute $\mathbf{U}_{(k+1)}^{n+1}$ by solving the fluid problem, using the newly computed fluid domain and the structure displacement at previous iteration to provide suitable boundary data at the interface:
$$\begin{cases} \mathbb{F}_f(\mathbf{U}_{(k+1)}^{n+1}, \mathbf{G}_{(k+1)}^{n+1}) = \mathbf{0} \,, \\ \mathbb{C}_f(\mathbf{D}_{(k)}^{n+1}, \mathbf{U}_{(k+1)}^{n+1}, \mathbf{G}_{(k+1)}^{n+1}) = \mathbf{0} \,; \end{cases}$$

3. compute $\widetilde{\mathbf{D}}_{(k+1)}^{n+1}$ by solving the structure problem, using the just computed fluid domain solution to provide suitable boundary data at the interface:
$$\begin{cases} \mathbb{S}_s(\widetilde{\mathbf{D}}_{(k+1)}^{n+1}) = \mathbf{0} \,, \\ \mathbb{C}_s(\widetilde{\mathbf{D}}_{(k+1)}^{n+1}, \mathbf{U}_{(k+1)}^{n+1}, \mathbf{G}_{(k+1)}^{n+1}) = \mathbf{0} \,; \end{cases}$$

10

4. apply relaxation or acceleration to the structure displacement, by setting

$$\mathbf{D}_{(k+1)}^{n+1} = \mathbb{R}_{(k+1)}(\widetilde{\mathbf{D}}_{(k+1)}^{n+1}, \mathbf{D}_{(k)}^{n+1}, \mathbf{D}_{(k-1)}^{n+1}, \dots) \ .$$

We use the same stopping criterion as for PE schemes.

This type of scheme is depicted in Figure 2b. As before, different schemes are obtained by making different choices for the interface conditions $\mathbb{C}_f$ and $\mathbb{C}_s$.

We remark that other types of schemes with implicit geometric coupling can be obtained e.g. by performing two nested loops at each timestep: in the outer loop, the geometry problem is solved and the fluid domain updated, and in the inner loop the fluid and structure problems are solved for a fixed fluid domain [68]. Moreover, an intermediate approach in this context is obtained by performing a small, fixed number of iterations on the outer loop for the domain displacement [68].

4.2   Monolithic (M) schemes

Now, we consider schemes based on solving in a single shot the algebraic nonlinear system arising from the time and space discretization of the FSI problem. We employ the Newton scheme for the linearization of such system. With this purpose, let us rewrite (6) in the following more compact form:

$$\begin{cases} \mathbb{G}(\mathbf{G}^{n+1}, \mathbf{D}^{n+1}) = \mathbf{0} \ , \\ \mathbb{F}(\mathbf{G}^{n+1}, \mathbf{U}^{n+1}, \mathbf{D}^{n+1}) = \mathbf{0} \ , \quad n = 0, 1, 2, \dots, N_t \ , \\ \mathbb{S}(\mathbf{G}^{n+1}, \mathbf{U}^{n+1}, \mathbf{D}^{n+1}) = \mathbf{0} \ , \end{cases} \tag{7}$$

where $\mathbb{G}$ includes both $\mathbb{G}_f$ and the boundary conditions for the fluid domain displacement, $\mathbb{F}$ includes $\mathbb{F}_f$ and $\mathbb{C}_k$ and $\mathbb{S}$ includes $\mathbb{S}_s$ and $\mathbb{C}_d$ (see Appendix A for the explicit definition of the operators).

4.2.1   Monolithic scheme with explicit geometric coupling (ME)

Given $\mathbf{G}^n$, $\mathbf{D}^n$ and $\mathbf{U}^n$, to compute the solution at timestep $n+1$:

1. compute $\mathbf{G}^{n+1}$ by solving the fluid domain displacement problem, using the structure displacement at previous time step:
$$\begin{cases} \mathbb{G}_f(\mathbf{G}^{n+1}) = \mathbf{0} \ , \\ \mathbb{C}_g(\mathbf{G}^{n+1}, \mathbf{D}^n) = \mathbf{0} \ , \end{cases}$$
and update the fluid domain according to the newly computed fluid domain displacement;

2. solve the fluid-structure coupled problem with a Newton loop: set $\mathbf{U}_{(0)}^{n+1} = \mathbf{U}^n$ and $\mathbf{D}_{(0)}^{n+1} = \mathbf{D}^n$, then for $k = 0, 1, 2, \dots$ and until convergence,

$$J_{\text{FS}}(\mathbf{G}^{n+1}, \mathbf{U}_{(k)}^{n+1}, \mathbf{D}_{(k)}^{n+1}) \begin{bmatrix} \delta \mathbf{U} \\ \delta \mathbf{D} \end{bmatrix} = \mathbf{R}(\mathbf{G}^{n+1}, \mathbf{U}_{(k)}^{n+1}, \mathbf{D}_{(k)}^{n+1}) \ , \tag{8}$$

$$\mathbf{U}_{(k+1)}^{n+1} = \mathbf{U}_{(k)}^{n+1} - \delta \mathbf{U} \ ,$$
$$\mathbf{D}_{(k+1)}^{n+1} = \mathbf{D}_{(k)}^{n+1} - \delta \mathbf{D} \ ,$$

where

$$J_{\text{FS}} = \begin{bmatrix} \dfrac{d\mathbb{F}}{d\mathbf{U}^{n+1}} & \dfrac{d\mathbb{F}}{d\mathbf{D}^{n+1}} \\ \dfrac{d\mathbb{S}}{d\mathbf{U}^{n+1}} & \dfrac{d\mathbb{S}}{d\mathbf{D}^{n+1}} \end{bmatrix} \qquad \mathbf{R} = \begin{bmatrix} \mathbb{F} \\ \mathbb{S} \end{bmatrix}$$

We remark that in the computation of $\mathbf{R}$ and J_{FS} the last available fluid domain displacement, $\mathbf{G}^{n+1}$ is used.
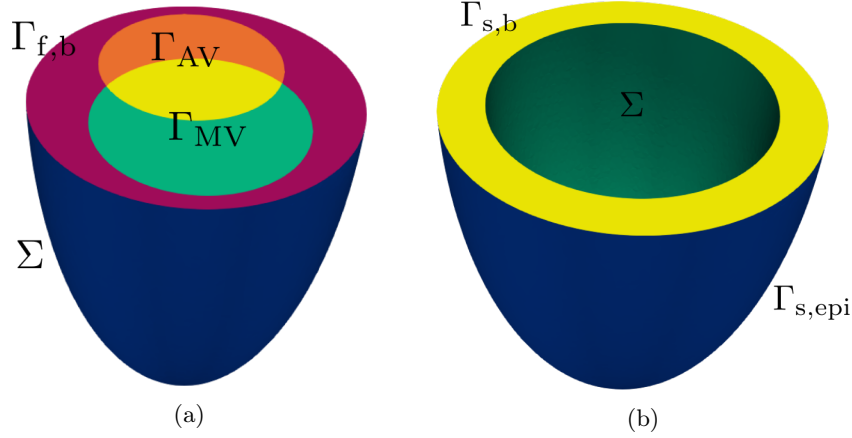
Figure 3: Fluid (a) and structure (b) meshes for the prolate ellipsoid (tests A, B and C).

4.2.2 Monolithic scheme with implicit geometric coupling (MI)

To obtain a scheme with implicit geometric coupling, it is possible to update the fluid domain displacement within the Newton loop, resulting in a scheme in which the fluid domain displacement is treated implicitly. Given $\mathbf{G}^n$, $\mathbf{D}^n$ and $\mathbf{U}^n$, to compute the solution at timestep $n+1$ set $\mathbf{G}^{n+1}_{(0)} = \mathbf{G}^n$, $\mathbf{U}^{n+1}_{(0)} = \mathbf{U}^n$ and $\mathbf{D}^{n+1}_{(0)} = \mathbf{D}^n$, then iterate for $k = 0, 1, 2, \ldots$ until convergence:

1. compute $\mathbf{G}^{n+1}_{(k+1)}$ by solving the fluid domain displacement problem, using the structure displacement at previous iteration:

$$\begin{cases} \mathbb{G}_{\mathrm{f}}(\mathbf{G}^{n+1}_{(k+1)}) = \mathbf{0} \ , \\ \mathbb{C}_{\mathrm{g}}(\mathbf{G}^{n+1}_{(k+1)}, \mathbf{D}^{n+1}_{(k)}) = \mathbf{0} \ , \end{cases}$$

and update the fluid domain according to the newly computed fluid domain displacement;

2. compute $\mathbf{U}^{n+1}_{(k+1)}$ and $\mathbf{D}^{n+1}_{(k+1)}$ with a Newton step:

$$J_{\mathrm{FS}}(\mathbf{G}^{n+1}_{(k+1)}, \mathbf{U}^{n+1}_{(k)}, \mathbf{D}^{n+1}_{(k)}) \begin{bmatrix} \delta\mathbf{U} \\ \delta\mathbf{D} \end{bmatrix} = \mathbf{R}(\mathbf{G}^{n+1}_{(k+1)}, \mathbf{U}^{n+1}_{(k)}, \mathbf{D}^{n+1}_{(k)}) \ ,$$

$$\mathbf{U}^{n+1}_{(k+1)} = \mathbf{U}^{n+1}_{(k)} - \delta\mathbf{U} \ ,$$

$$\mathbf{D}^{n+1}_{(k+1)} = \mathbf{D}^{n+1}_{(k)} - \delta\mathbf{D} \ .$$

This corresponds to solving the fully coupled system (7) with an inexact-Newton approach, in which the Jacobian terms involving derivatives with respect to the fluid domain displacement (i.e. the shape derivatives [17, 35]) are neglected.

4.2.3 Preconditioning

In both the ME and the MI schemes, the linear systems to be solved are the one arising from the ALE lifting problem, which is preconditioned by means of algebraic multigrid (AMG) [49], and a linear system with fluid and structure unknowns, with the general block structure

$$J = \begin{bmatrix} J_{\mathrm{ff}} & J_{\mathrm{fs}} \\ J_{\mathrm{sf}} & J_{\mathrm{ss}} \end{bmatrix} \ . \tag{9}$$
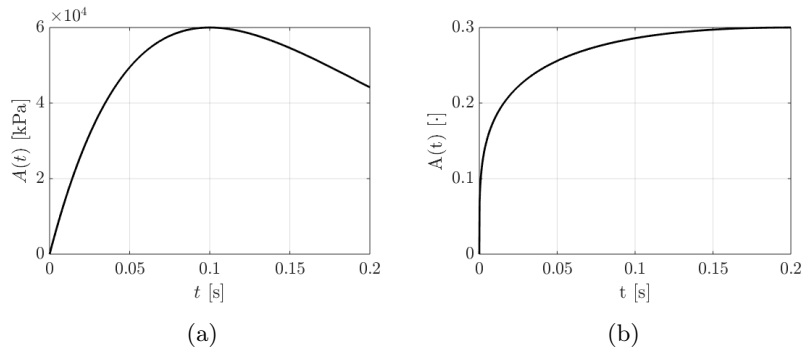
Figure 4: Analytical activation functions for the active stress (a) and active strain (b) test cases.

A possible way to precondition (9) is to use a block lower triangular preconditioner:

$$P = \begin{bmatrix} J_{\text{ff}} & 0 \\ J_{\text{sf}} & J_{\text{ss}} \end{bmatrix} .$$

The inverse of P is

$$P^{-1} = \begin{bmatrix} J_{\text{ff}}^{-1} & 0 \\ -J_{\text{ss}}^{-1} J_{\text{sf}} J_{\text{ff}}^{-1} & J_{\text{ss}}^{-1} \end{bmatrix} .$$

The inverse of fluid and structure blocks, required by the application of P^{-1}, is approximated by means of suitable inner preconditioners. For the fluid block (both velocity and pressure variables), we make use of the SIMPLE preconditioner P_{SIMPLE} [31]. For the structure block, we employ an AMG preconditioner P_{s}, whence

$$P_{\text{FSI}}^{-1} = \begin{bmatrix} P_{\text{SIMPLE}}^{-1} & 0 \\ -P_{\text{s}}^{-1} J_{\text{sf}} P_{\text{SIMPLE}}^{-1} & P_{\text{s}}^{-1} \end{bmatrix} .$$

The application of P_{FSI}^{-1} can be expressed in terms of one application of the SIMPLE preconditioner, one application of the AMG preconditioner for the structure, and a few matrix-vector multiplications.

Other preconditioners can be derived similarly, e.g. by resorting to a block LU factorization of matrix (9) [30] or using a block upper triangular or block diagonal preconditioners. Among these options, we found the block lower triangular preconditioner to perform slightly better than the others in terms of overall computational cost.

5   Numerical results

We present numerical results on FSI test cases. We aim at comparing the performance of the coupling schemes presented, in terms of overall computational costs and, for partitioned schemes, number of iterations required for convergence. We will consider idealized problems in the context of cardiovascular haemodynamics. In all cases we will assume the solid to have density $\rho_{\text{s}} = 1000 \, \text{kg/m}^3$, and the fluid to have density $\rho_{\text{f}} = 1060 \, \text{kg/m}^3$ and viscosity $\mu = 3.5 \cdot 10^{-3} \, \text{Pa} \cdot \text{s}$.

For each test, we consider the ME (Section 4.2.1) and MI (Section 4.2.2) schemes, as well as DN and RN partitioned schemes with static relaxation (13), Aitken acceleration (14) and Anderson acceleration.

Simulations were carried out using life$^{\text{x}}$ [3], a C++ library developed in-house, tailored to cardiac applications, based on the finite element library deal.II [2, 7, 8]. All the simulations ran on 48 cores from CINECA GALILEO100 [1].

<table>
<tr><td>(a) $t = 0\,\mathrm{ms}$</td><td>(b) $t = 100\,\mathrm{ms}$</td><td>(c) $t = 200\,\mathrm{ms}$</td></tr>
</table>

velocity magnitude [m/s]

0   0.2   0.4   0.6   0.8   1

pressure [mmHg]
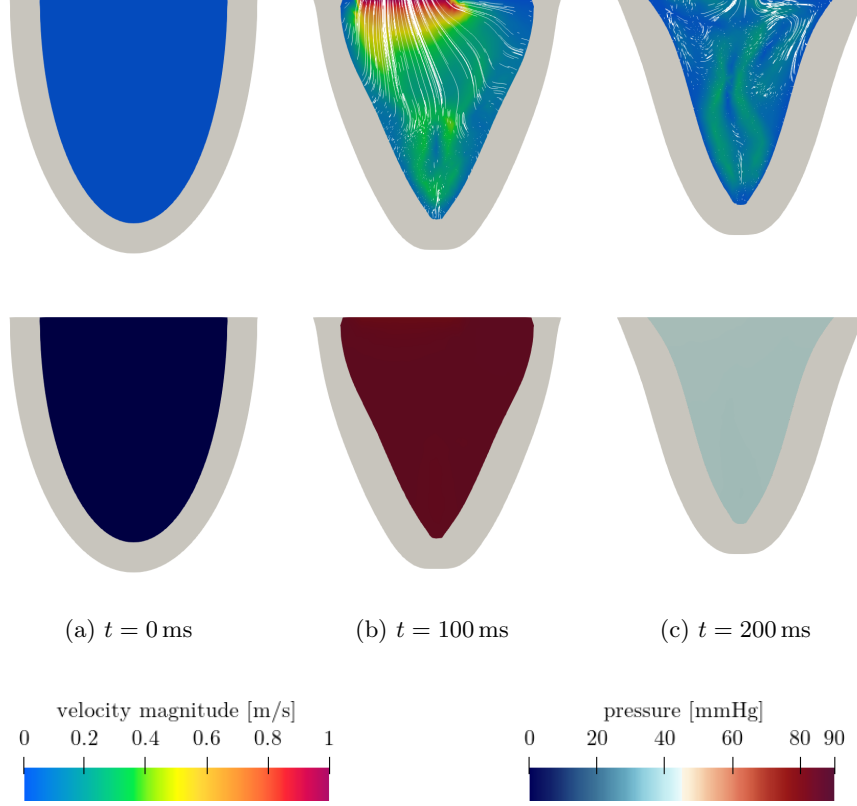
0   20   40   60   80 90

Figure 5: Snapshots of the fluid velocity (top) and pressure (bottom) of the idealized ventricle test case, in systole with the active stress formulation (test A1).

5.1 Test A: idealized left ventricle in systole

We consider an idealized left ventricle shaped as a prolate ellipsoid. The corresponding fluid and structure computational domains are represented in Figure 3, left and right respectively. On the top surface of the fluid domain, we identify two intersecting circular regions Γ_{AV}, Γ_{MV} that represent in this idealized context the aortic and mitral valve orifice, respectively, similarly to the test case considered in [91] for a CFD ventricular simulation. In this test case, we reproduce the systolic phase during which the ventricle contracts and blood is ejected through the aortic valve. Therefore, we impose the no-slip condition $\mathbf{u} = \mathbf{0}$ on $\Gamma_{\mathrm{MV}} \backslash \Gamma_{\mathrm{AV}}$ and on $\Gamma_{\mathrm{f,b}}$, and a resistance boundary condition on Γ_{AV} [40, 91]:

$$\sigma_{\mathrm{f}} \mathbf{n} = - \left(p_0 + R \int_{\Gamma_{\mathrm{AV}}} \mathbf{u} \cdot \mathbf{n} d\Gamma \right) \mathbf{n} \qquad \text{on } \Gamma_{\mathrm{AV}} , \tag{10}$$

where $p_0 = 6000\,\mathrm{Pa}$ represents the minimum aortic pressure and $R = 1 \cdot 10^7\,\mathrm{kg/(s \cdot m^4)}$ is a resistance parameter, calibrated in accordance with [79]. We impose a no-slip condition $\mathbf{u} = \mathbf{0}$ on $\Gamma_{\mathrm{f,b}}$ as well.

The material model of the solid is the Guccione law (2). As boundary conditions for the structure problem, we use a homogeneous Dirichlet condition $\mathbf{d} = \mathbf{0}$ on the base $\Gamma_{\mathrm{s,b}}$, and consistently keep the fluid domain base fixed, that is we impose $\mathbf{d}_{\mathrm{f}} = \mathbf{0}$ on $\Gamma_{\mathrm{f,b}} \cup \Gamma_{\mathrm{AV}} \cup \Gamma_{\mathrm{MV}}$. We remark that this condition is not physiological, but in this simplified test case avoids issues related to having moving inlet or outlet sections for the fluid. In a more realistic case, boundary conditions allowing for the displacement of the structure base should be employed, such as Robin boundary conditions [40] or more sophisticated conditions modeling the presence of the neglected part of the ventricle [80, 81].

(a) $t = 0\,\mathrm{ms}$ (b) $t = 100\,\mathrm{ms}$ (c) $t = 200\,\mathrm{ms}$

velocity magnitude [m/s]

0   0.2   0.4   0.6   0.8   1
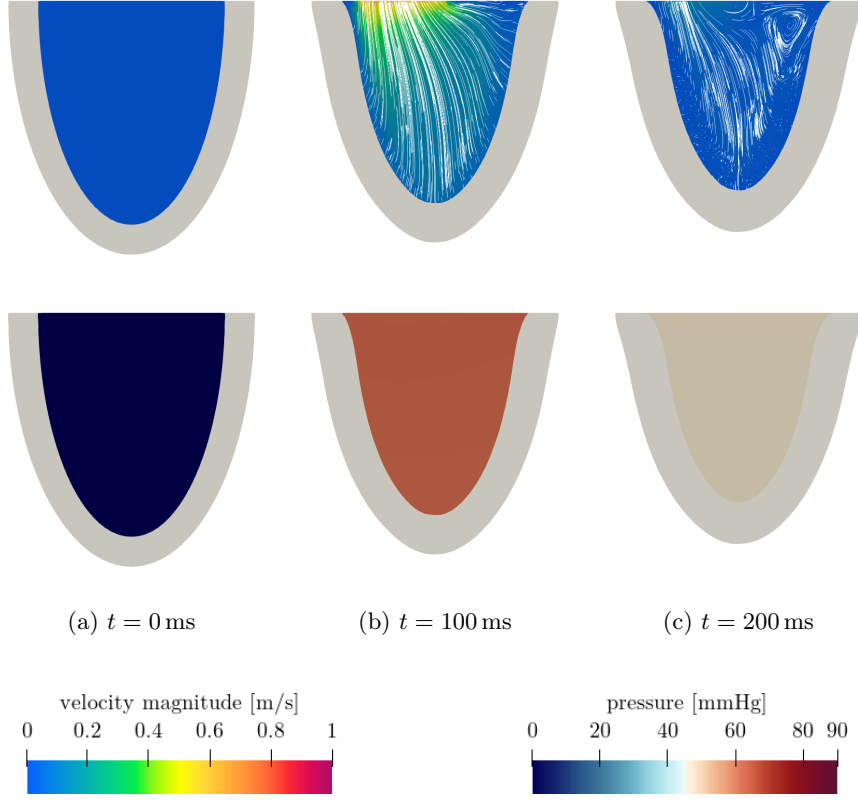
pressure [mmHg]

0   20   40   60   80   90

Figure 6: Snapshots of the fluid velocity (top) and pressure (bottom) of the idealized ventricle test case, in systole with the active strain formulation (test A2).

Finally, on the epicardium $\Gamma_{\mathrm{s,epi}}$ of the ventricle, we impose generalized Robin boundary conditions that mimic the presence of the pericardium, a sac containing the heart [40, 73, 80, 89]:

$$P(\mathbf{d})\mathbf{n} = -(\mathbf{n} \otimes \mathbf{n})\left(K_\perp \mathbf{d} + C_\perp \frac{\partial \mathbf{d}}{\partial t}\right) - (I - \mathbf{n} \otimes \mathbf{n})\left(K_\parallel \mathbf{d} + C_\parallel \frac{\partial \mathbf{d}}{\partial t}\right) , \qquad (11)$$

in which $K_\perp$, $K_\parallel$ are constant elasticty coefficients for the directions normal and parallel to the boundary respectively, and $C_\perp$ and $C_\parallel$ are constant viscosity coefficients for the directions normal and parallel to the boundary.

We run two tests in this setting, prescribing active contraction in the active stress formulation in one case (test A1) and in the active strain formulation in the other (test A2). The active contraction of the myocardium is achieved by defining the active stress or strain to be constant in space and variable in time according to a prescribed analytical function. Similarly to what done in [71], we choose a function of the form

$$A(t) = \begin{cases} 0 & t < t_0 , \\ A_{\mathrm{max}}\left(\dfrac{t - t_0}{T}\right)^p \exp\left\{p\left(1 - \dfrac{t - t0}{T}\right)\right\} & t \geq t_0 , \end{cases} \qquad (12)$$

where t_0 is the time at which contraction starts, T is the time of activation peak and p is a positive parameter. The graph of $A(t)$ is shown in Figure 4. For the active stress test case, we choose $t_0 = 0\,\mathrm{s}$, $T = 0.1\,\mathrm{s}$, $A_{\mathrm{max}} = 60\,\mathrm{kPa}$ and $p = 1$. For the active strain test case we use $t_0 = 0\,\mathrm{s}$, $T = 0.2\,\mathrm{s}$, $A_{\mathrm{max}} = 0.3$ and $p = 0.25$. These values do not lead to physiological deformations of the idealized

	CPU time [s]		Fixed-point iterations		
Scheme	total	assembly	min.	avg.	max.
ME	6850	4270	-	-	-
PE-DN-SR		CPU time $> 24\,$h			
PE-DN-AitA		convergence failure			
PE-DN-AndA		convergence failure			
PE-RN-SR		CPU time $> 24\,$h			
PE-RN-AitA	60120	28300	13	15.6	17
PE-RN-AndA	54090	25500	13	14.0	15
MI	16500	4262	-	-	-
PI-DN-SR		CPU time $> 24\,$h			
PI-DN-AitA		convergence failure			
PI-DN-AndA		convergence failure			
PI-RN-SR		CPU time $> 24\,$h			
PI-RN-AitA	74890	34770	14	15.9	18
PI-RN-AndA	58180	26980	13	14.2	15

Table 1: Performance of the different schemes for the systole test case with active stress formulation (test A1). For each scheme we report the total CPU time required for the solution of the test case, as well as the time spent assembling linear systems; for fully coupled partitioned schemes we also report the minimum, average and maximum across timesteps of the number of iterations required for convergence.

ventricle, but are chosen so that the resulting velocities, both of the myocardium and of the blood, have the same orders of magnitude that can be expected in a physiological simulation.

Due to the nonlinearity and anisotropy of the contitutive law of the solid structure, optimal relaxation and acceleration parameters are not available. They were tuned so as to obtain convergence, although it is worth observing that tuning parameters is itself a major issue with these schemes. The same argument holds true for RN schemes as well. Although optimal values of the parameter α_{f} have been studied for sperical geometries and linear elasticity in [42], their application here is not trivial due to the non-linearity of the structure. More investigations are needed on this point.

The solution at a few time instants is reported in Figures 5 and 6, and the computational times associated to the different coupling schemes are reported in Tables 1 and 2.

Partitioned schemes with static relaxation require more time than 24 h to converge, except for RN in the active strain test case. The DN scheme fails to converge with all acceleration schemes, for explicit and implicit geometric coupling, and in both the active stress and active strain cases. Conversely, the RN scheme converges successfully when using Aitken and Anderson acceleration, with Anderson acceleration slightly improving over Aitken acceleration. In all cases considered the monolithic approach was several times faster than any of the partitioned schemes. The MI scheme is more costly than its explicit counterpart, while no significant increase in number of iterations is observed for RN schemes with implicit geometric coupling. No relevant difference is observed between the active stress and active strain approaches, in terms of relative efficiency of the monolithic and partitioned schemes.

5.2 Test B: idealized left ventricle in diastole

In this case we use the same geometry as described for the systole. Boundary conditions on the structure and on the fluid domain are also the same. For the fluid problem, we impose an inlet condition through Γ_{MV}, to reproduce the diastolic filling of the ventricle. In particular, we set $\sigma_{\mathrm{f}}\mathbf{n} = -p_{\mathrm{MV}}\mathbf{n}$ on Γ_{MV}, with $p_{\mathrm{MV}} = 1333\,$Pa. Conversely, we set $\mathbf{u} = \mathbf{0}$ on $\Gamma_{\mathrm{AV}}\backslash\Gamma_{\mathrm{MV}}$ and on $\Gamma_{\mathrm{f,b}}$. Since during diastole the ventricle is relaxing, we do not prescribe any activation.

We remark that the initial conditions of this test case are not consistent with end-systolic conditions

	CPU time [s]		Fixed-point iterations		
Scheme	total	assembly	min.	avg.	max.
ME	7230	4090	-	-	-
PE-DN-SR		CPU time $> 24\,\mathrm{h}$			
PE-DN-AitA		convergence failure			
PE-DN-AndA		convergence failure			
PE-RN-SR	79110	36090	19	20.5	25
PE-RN-AitA	46920	21300	11	12.1	21
PE-RN-AndA	46380	21000	11	11.8	14
MI	17100	8790	-	-	-
PI-DN-SR		CPU time $> 24\,\mathrm{h}$			
PI-DN-AitA		convergence failure			
PI-DN-AndA		convergence failure			
PI-RN-SR	79340	36260	19	20.4	24
PI-RN-AitA	50020	22400	11	12.5	22
PI-RN-AndA	48760	21630	11	12.3	14

Table 2: Performance of the different schemes for the systole test case with active strain formulation (test A2). For each scheme we report the total CPU time required for the solution of the test case, as well as the time spent assembling linear systems; for fully coupled partitioned schemes we also report the minimum, average and maximum across timesteps of the number of iterations required for convergence.

as found at the end of the previous test case. The aim of this test is to assess the performance of the algorithms in the context of a slow inflow and in absence of the active contraction, rather than providing physiologically meaningful insight.

A few snapshots of the solution are reported in Figure 7, and computational times for the different schemes are reported in Table 3. From there, it is again evident that the monolithic approach outperforms the partitioned approach, both with an explicit and with an implicit treatment of the geometry, even during the relatively slow diastolic phase.

5.3 Test C: idealized left ventricle, full heartbeat

In this test we assess the reliability of the ME scheme for the simulation of a full heartbeat on an idealized ventricle geometry. This is of particular interest since specific features arise when both systolic and diastolic are considered. In particular, during the heartbeat, the opening and closing of valves determine four distinct phases [57]:

- isovolumetric contraction; both valves are closed; the ventricle starts contracting, resulting in a rapid increase of ventricular pressure; when the pressure inside the chamber becomes larger than that of the aorta, the aortic valve opens and ejection phase begins;

- ejection; the aortic valve is open, and the mitral valve is closed; blood exits from the ventricle into the aorta. The aortic valve closes to prevent reverse flow, starting the isovolumetric relaxation phase;

- isovolumetric relaxation; both valves are closed, and the ventricle relaxes, resulting in the decrease of ventricular pressure; when the pressure falls below the atrial pressure, mitral valve opens and the filling phase starts;

- filling; the mitral valve is open, and the aortic valve is closed; blood flows from the atrium into the ventricle, increasing its volume; the mitral valve closes to prevent reverse flow, and a new isovolumetric contraction phase begins.
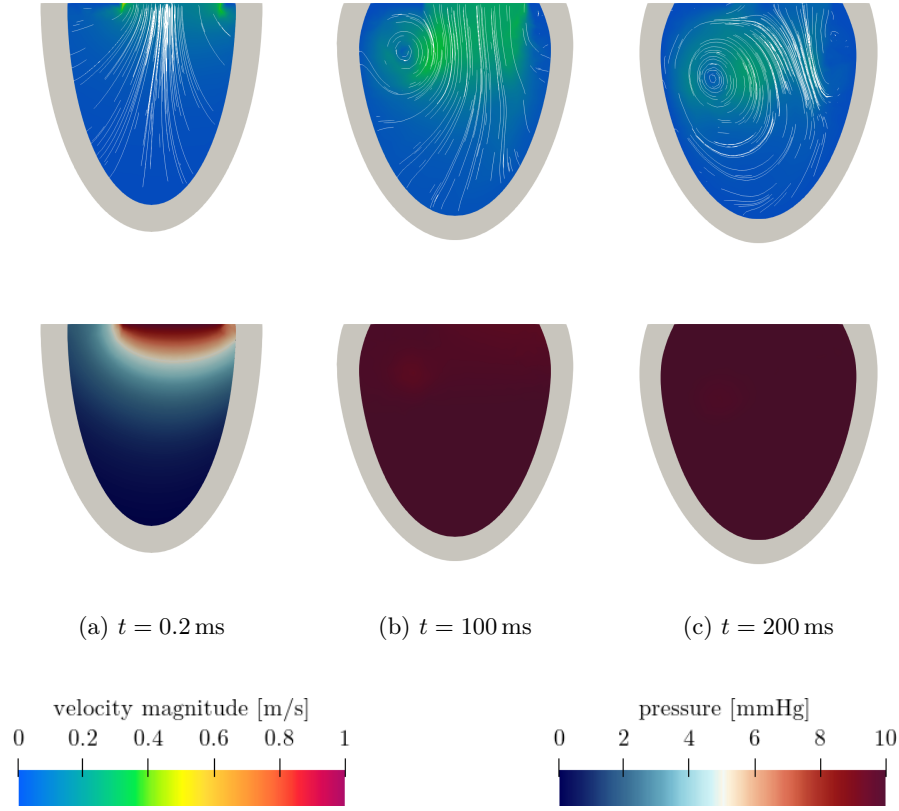
(a) $t = 0.2\,\text{ms}$ (b) $t = 100\,\text{ms}$ (c) $t = 200\,\text{ms}$

velocity magnitude [m/s]

0   0.2   0.4   0.6   0.8   1

pressure [mmHg]

0   2   4   6   8   10

Figure 7: Snapshots of the fluid velocity (top) and pressure (bottom) of the idealized ventricle test case, in diastole (test B).

| Scheme | CPU time [s] | | Fixed-point iterations | | |
	total	assembly	min.	avg.	max.
ME	6560	3830	-	-	-
PE-DN-SR	CPU time > 24 h				
PE-DN-AitA	convergence failure				
PE-DN-AndA	convergence failure				
PE-RN-SR	CPU time > 24 h				
PE-RN-AitA	50050	22677	12	14.1	15
PE-RN-AndA	46650	21235	12	13.4	14
MI	10900	6150	-	-	-
PI-DN-SR	CPU time > 24 h				
PI-DN-AitA	convergence failure				
PI-DN-AndA	convergence failure				
PI-RN-SR	CPU time > 24 h				
PI-RN-AitA	50870	22780	12	14.0	15
PI-RN-AndA	49700	22168	12	13.7	14

Table 3: Performance of the different schemes for the diastole test case (test B). For each scheme we report the total CPU time required for the solution of the test case, as well as the time spent assembling linear systems; for fully coupled partitioned schemes we also report the minimum, average and maximum across timesteps of the number of iterations required for convergence.
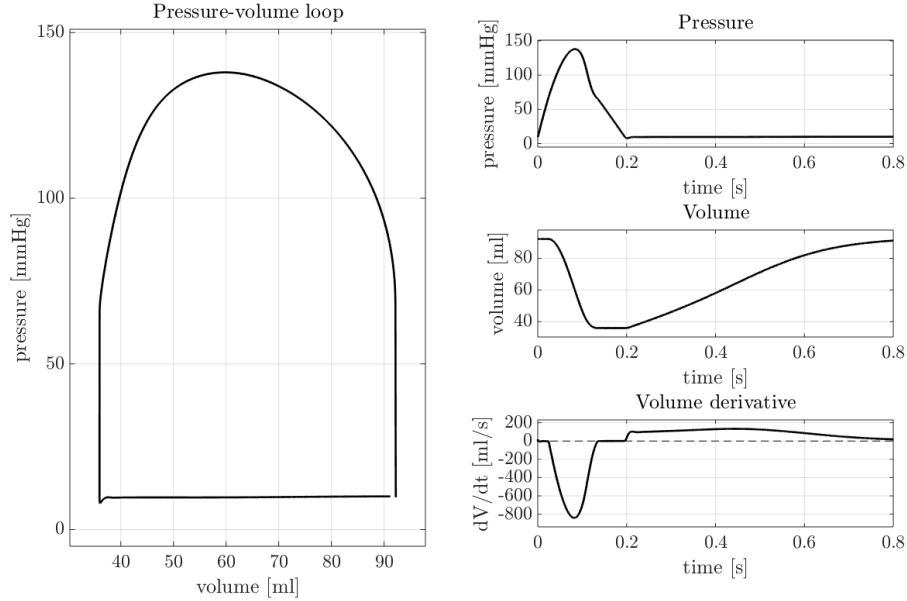
Figure 8: Pressure and volume plots of the full heartbeat test case (test C).

We reproduce these phases by switching the boundary conditions applied on Γ_{AV} and Γ_{MV} according to the ventricular pressure and to the flow through the valve orifices. Specifically, we represent open valves with the resistance condition (10) for the aortic valve and the Neumann condition for the mitral valve, and closed valves with the no-slip condition $\mathbf{u} = \mathbf{0}$. Valves are opened according to the average pressure $\bar{p}$ in the fluid domain: the aortic valve is opened when $\bar{p} \geq p_{\mathrm{AV}}$, and the mitral valve when $\bar{p} \leq p_{\mathrm{MV}}$. Conversely, valves are closed when reverse flow occurs through their section.

With respect to previous tests, we also change boundary and initial conditions. On the ventricular base of the structure, we impose a Robin-like condition as in (11), to allow for the base to move towards the apex as the ventricle contracts, as is the case in healthy hearts. We remark that this leads inlet and outlet boundaries for the fluid domain to move, and this can be problematic in more complex test cases with realistic geometries. Moreover, we start the simulation by inflating the structure with a pressure of $1333\,\mathrm{Pa}$, roughly corresponding to the pressure at the end of the diastolic phase. This allows to start from a more realistic initial condition.

We use an active stress formulation for active mechanics. The final simulation time is $T = 0.8\,\mathrm{s}$, and we set $\Delta t = 2 \cdot 10^{-4}\,\mathrm{s}$. Overall, the total CPU time needed for the simulation was $14\,\mathrm{h}$.

We report ventricular volume and pressure in Figure 8. The evolution of volume and pressure is qualitatively consistent with the behavior of a normal human heart [57]. Some snapshots of the solution are shown in Figures 9 and 10. It can be seen how the ventricle deforms and contracts during systole by shortening and thickening, and how the original volume and shape are recovered at the end of the heartbeat, after relaxation.

It is worth remarking that this simplified model includes isovolumetric phases of the heartbeat, as can be seen from Figure 8. Such phases are usually neglected in purely CFD simulations, in which the endocardial wall displacement is provided as data [37, 91, 94]. Indeed, because of the fluid incompressibility and the fact that both valves are closed, in isovolumetric phases prescribing a Dirichlet condition on the whole boundary would generally be incompatible with the divergence-free constraint. As a matter of fact, Dirichlet data should satisfy a compatibility condition [76], often not satisfied by noisy imaging[1]. Moreover, pressure would be defined only up to a constant, in that setting. Therefore,

---

[1]Notice that this is true only for physiological cases, where the valves are perfectly closed. In regurgitant cases, such

(a) $t = 0\,\text{ms}$ (b) $t = 5\,\text{ms}$ (c) $t = 10\,\text{ms}$

(d) $t = 25\,\text{ms}$ (e) $t = 35\,\text{ms}$ (f) $t = 75\,\text{ms}$

velocity $[\text{m/s}]$
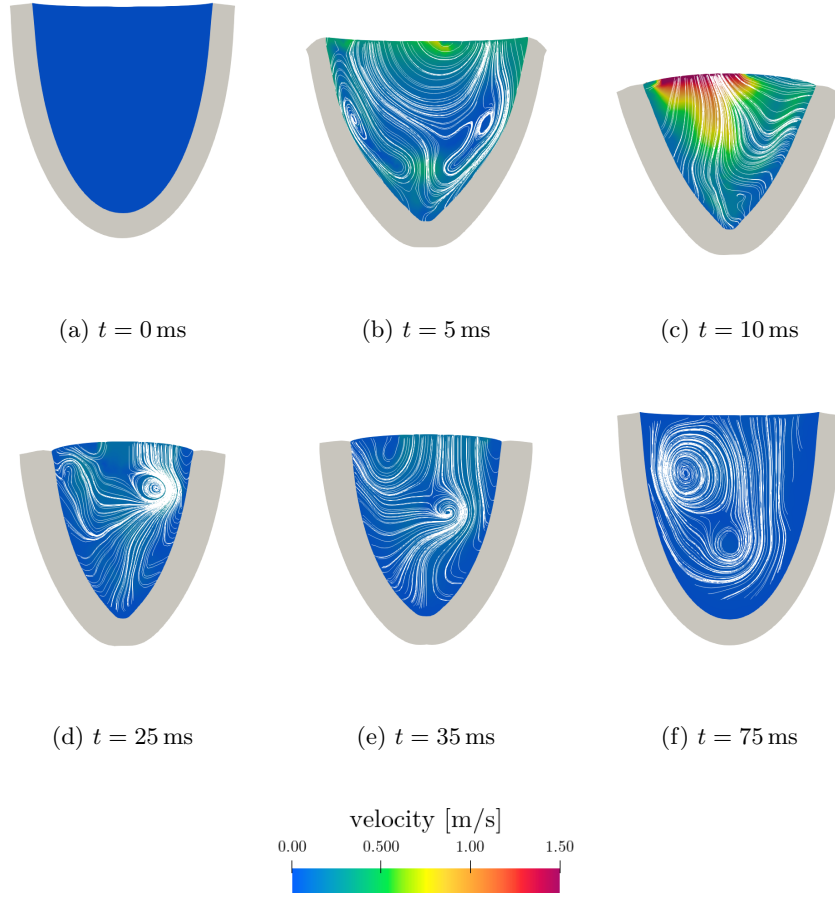
0.00   0.500   1.00   1.50

Figure 9: Snapshots of the fluid velocity of the idealized ventricle test case, for the full heartbeat (test C).

isovolumetric phases cannot be treated in a CFD model, unless special techniques are implemented to obtain a well-posed problem [94]. An FSI model is instead capable of representing isovolumetric phases [71, 94], thanks to the fact that the velocity at the endocardial wall is not known from data but is itself an unknown of the problem, and the model also accounts for the stresses exchanged at the fluid-structure interface.

However, after time and space discretizations, in our computational model the fluid volume is not exactly preserved over time. This is due mostly to two different sources of spurious volume variations:

- explicit treatment of the geometry: the use of the structure displacement at previous timestep to compute the fluid domain at current timestep leads to a mismatch between the fluid volume and the fluid velocity at the boundary;

- SUPG stabilization terms: these can be interpreted as artificial compressibility, so that at the discrete level the fluid is not strictly incompressible, and a small variation in volume is observed.

Both effects reduce as $\Delta t \to 0$. Moreover, the volume variations that they introduce are several orders of magnitude smaller than the characteristic variations in volume of the ventricle over a heartbeat: in

---

as mitral valve regurgitation, a Neumann boundary would appear in correspondence of the regurgitation orifice.

(a) $t = 0 \, \text{ms}$ (b) $t = 5 \, \text{ms}$ (c) $t = 10 \, \text{ms}$

(d) $t = 15 \, \text{ms}$ (e) $t = 35 \, \text{ms}$ (f) $t = 75 \, \text{ms}$

pressure

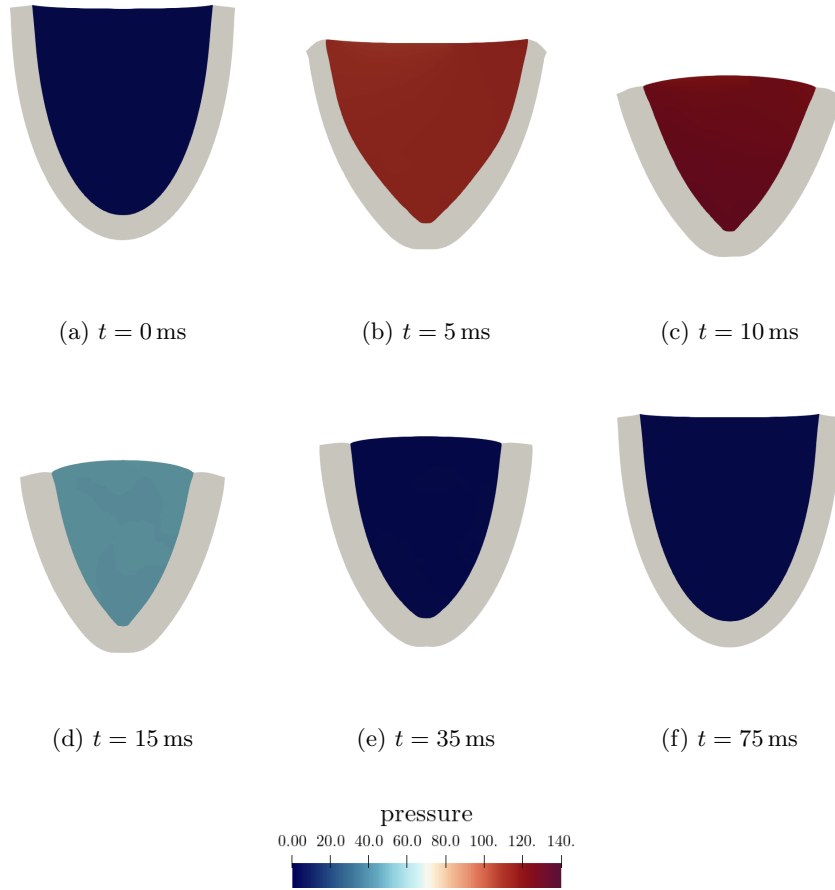0.00   20.0   40.0   60.0   80.0   100.   120.   140.

Figure 10: Snapshots of the fluid pressure of the idealized ventricle test case, for the full heartbeat (test C).

this test case, during isovolumetric contraction, the total volume variation was of $0.07 \, \text{ml}$, corresponding to $0.075 \, \%$ of the initial volume. Overall, these spurious effects can be considered negligible.

6   Conclusions

In the context of FSI heart modeling, we compare in a systematic way fully coupled partitioned and monolithic FSI coupling schemes on benchmark cases that mimic, in an idealized setting, the flow regime characteristic of a human ventricle. For all the cases considered, the performance of the monolithic scheme was significantly better than that of partitioned iterations, resulting in a total computational time several times smaller for the whole heartbeat simulation. Partitioned schemes based on Dirichlet-Neumann interface conditions suffer from convergence issues, and have proven to be impractical for the cardiac tests. Robin-Neumann schemes performed slightly better, and benefit from acceleration methods, but they still require parameter tuning to be used effectively. For the complex geometries and material models characterizing the heart, this tuning is not trivial. Conversely, the monolithic approach is parameter-free, and is consequently more robust and flexible.

In the monolithic approach, using an implicit discretization for fluid domain displacement entails a higher computational cost than using an explicit discretization. Fully coupled partitioned schemes, on

the contrary, have similar costs with both explicit and implicit geometric coupling. Nonetheless, the monolithic scheme is more efficient than the partitioned ones even if an implicit geometric coupling is used. We also found that Anderson acceleration is capable of slightly improving the results of partitioned schemes. Moreover, the relative performance of the schemes does not vary depending on the choice of active mechanics formulation: indeed, with both with active stress and active strain formulations, the monolithic scheme performed significantly faster than the partitioned ones.

Finally, using the monolithic scheme, we run a simulation of a full heartbeat on the idealized geometry, switching inlet and outlet boundary conditions to simulate in a simplified way the opening and closing of cardiac valves. This test case shows the ability of the computational model to replicate a full heartbeat. In particular, we reproduce the isovolumetric phases, which is a challenge in other simulation settings involving three dimensional modeling of the cardiac blood flow.

Overall, this study indicates that, for strongly coupled FSI simulations in the cardiac context, a monolithic approach seems to be preferrable to a partitioned one, thanks to its robustness and efficiency. However, more specific studies on the Robin interface parameters for the cardiac case are mandatory to improve the corresponding partitioned schemes.

7 Acknowledgements

A Definition of algebraic operators

In this section we will give the explicit definition of each of the operators introduced in Section 3. We will not give details on the derivation of the operators, as it follows the classical finite elements procedure, and refer the interested reader to [54, 76].

In the following, we shall use the subscripts f, s and Σ for the vectors $\mathbf{G}$, $\mathbf{D}$ and $\mathbf{U}$ to denote their entries that correspond to nodes located on the interior (not on the interface) of the fluid domain, on the interior of the structure domain and on the fluid-structure interface respectively.

We shall assume that the same discretization is used for the fluid domain displacement and fluid velocity, so that both are described using the same set of basis functions. We partition the basis functions as done for the solution vectors into a subset for interior nodes and a subset for interface nodes. We will denote the basis functions as follows:

- $\boldsymbol{\varphi}_{\mathrm{s},i}^{\mathrm{s}}$, for $i \in \{1, \ldots, N_{\mathrm{s}}^{\mathrm{s}}\}$, are the basis functions for the structure displacement corresponding to the interior nodes of the structure domain (i.e. such that their support does not intersect Σ);

- $\boldsymbol{\varphi}_{\Sigma,i}^{\mathrm{s}}$, for $i \in \{1, \ldots, N_{\Sigma}^{\mathrm{s}}\}$, are the basis functions for the structure displacement corresponding to the interface nodes of the structure domain (i.e. such that their support intersects Σ);

- $\boldsymbol{\varphi}_{\mathrm{f},i}^{\mathrm{f}}$, for $i \in \{1, \ldots, N_{\mathrm{f}}^{\mathrm{f}}\}$, are the basis functions for the fluid velocity and fluid domain displacement corresponding to the interior nodes of the fluid domain;

- $\boldsymbol{\varphi}_{\Sigma,i}^{\mathrm{f}}$, for $i \in \{1, \ldots, N_{\Sigma}^{\mathrm{f}}\}$, are the basis functions for the fluid velocity and fluid domain displacement corresponding to the interface nodes of the fluid domain;

- ψ_i, for $i \in \{1, \ldots, N^{\mathrm{P}}\}$, are the basis function for the fluid pressure.

We assume that the fluid and structure meshes are conforming, so that there exists a one-to-one correspondence between interface nodes on the two subdomains. This entails $N_{\Sigma}^{\mathrm{s}} = N_{\Sigma}^{\mathrm{f}}$. We will assume that the numbering of interface basis functions on the two subdomains is the same, so that $\boldsymbol{\varphi}_{\Sigma,i}^{\mathrm{s}} = \boldsymbol{\varphi}_{\Sigma,i}^{\mathrm{f}}$ on Σ.

A.1 Structure displacement

The operator $\mathbb{S}_{\mathrm{s}}$ is defined as

$$\mathbb{S}_{\mathrm{s}}(\mathbf{D}^{n+1}) = \frac{\rho_{\mathrm{s}}}{\Delta t} M_{\mathrm{ss}}^{\mathrm{s}}(\mathbf{D}_{\mathrm{s}}^{n+1} - 2\mathbf{D}_{\mathrm{s}}^{n} + \mathbf{D}_{\mathrm{s}}^{n-1}) + \frac{\rho_{\mathrm{s}}}{\Delta t} M_{\mathrm{s}\Sigma}^{\mathrm{s}}(\mathbf{D}_{\Sigma}^{n+1} - 2\mathbf{D}_{\Sigma}^{n} + \mathbf{D}_{\Sigma}^{n-1}) + K_{\mathrm{s}}^{\mathrm{s}}(\mathbf{D}^{n+1}) \, ,$$

where

$$M_{\mathrm{kl}}^{\mathrm{s}} \in \mathbb{R}^{N_{\mathrm{k}}^{\mathrm{s}} \times N_{\mathrm{l}}^{\mathrm{s}}} \qquad (M_{\mathrm{kl}}^{\mathrm{s}})_{i,j} = \int_{\widehat{\Omega}_{\mathrm{s}}} \boldsymbol{\varphi}_{\mathrm{k},i}^{\mathrm{s}} \cdot \boldsymbol{\varphi}_{\mathrm{l},j}^{\mathrm{s}} \qquad i \in \{1, \ldots, N_{\mathrm{k}}^{\mathrm{s}}\}, \ j \in \{1, \ldots, N_{\mathrm{l}}^{\mathrm{s}}\}, \qquad \mathrm{k,l} \in \{\mathrm{s}, \Sigma\}$$

are the structure mass matrix blocks corresponding to the different combinations of interior and interface basis functions, and

$$K_{\mathrm{k}}^{\mathrm{s}}(\mathbf{D}^{n+1}) \in \mathbb{R}^{N_{\mathrm{k}}^{\mathrm{s}}} \qquad (K_{\mathrm{k}}^{\mathrm{s}})_i = \int_{\widehat{\Omega}_{\mathrm{s}}} P(\mathbf{d}^{n+1}) : \nabla \boldsymbol{\varphi}_{\mathrm{k},i}^{\mathrm{s}} \qquad i \in \{1, \ldots, N_{\mathrm{k}}^{\mathrm{s}}\}, \qquad \mathrm{k} \in \{\mathrm{s}, \Sigma\}$$

is the nonlinear stiffness operator, corresponding to either the interior or interface basis functions.

A.2 Fluid domain displacement

The operators $\mathbb{G}_{\mathrm{f}}$ and $\mathbb{C}_{\mathrm{g}}$ are defined as

$$\mathbb{G}_{\mathrm{f}}(\mathbf{G}^{n+1}) = K_{\mathrm{ff}}^{\mathrm{g}}\mathbf{G}_{\mathrm{f}}^{n+1} + K_{\mathrm{f}\Sigma}^{\mathrm{g}}\mathbf{G}_{\Sigma}^{n+1} \, ,$$
$$\mathbb{C}_{\mathrm{g}}(\mathbf{G}^{n+1}, \mathbf{D}^{n+1}) = \mathbf{G}_{\Sigma}^{n+1} - \mathbf{D}_{\Sigma}^{n+1} \, ,$$

where

$$K_{\mathrm{kl}}^{\mathrm{g}} \in \mathbb{R}^{N_{\mathrm{k}}^{\mathrm{f}} \times N_{\mathrm{l}}^{\mathrm{f}}} \qquad (K_{\mathrm{kl}}^{\mathrm{g}})_{i,j} = \int_{\widehat{\Omega}_{\mathrm{f}}} \nabla \boldsymbol{\varphi}_{\mathrm{k},i}^{\mathrm{f}} : \nabla \boldsymbol{\varphi}_{\mathrm{l},j}^{\mathrm{f}} \qquad i \in \{1, \ldots, N_{\mathrm{k}}^{\mathrm{f}}\}, \ j \in \{1, \ldots, N_{\mathrm{l}}^{\mathrm{f}}\}, \qquad \mathrm{k,l} \in \{\mathrm{f}, \Sigma\} \, ,$$

are the stiffness matrix blocks corresponding to the different combinations of interior and interface basis functions. The operator $\mathbb{G}$ reads

$$\mathbb{G}(\mathbf{G}^{n+1}, \mathbf{D}^{n+1}) = \begin{bmatrix} \mathbb{G}(\mathbf{G}^{n+1}) \\ \mathbb{C}_{\mathrm{g}}(\mathbf{G}^{n+1}, \mathbf{D}^{n+1}) \end{bmatrix} \, .$$

A.3 Fluid problem

Let us denote by $\mathbf{V}$ and $\mathbf{P}$ the subset of fluid degrees of freedom $\mathbf{U}$ related to velocity and pressure respectively. The operator $\mathbb{F}_{\mathrm{f}} = \left[\mathbb{F}_{\mathrm{f}}^{\mathrm{U}}, \mathbb{F}_{\mathrm{f}}^{\mathrm{P}}\right]^{T}$ has two blocks, corresponding to the discretization of the momentum and incompressibility equations respectively. The first block reads:

$$\mathbb{F}_{\mathrm{f}}^{\mathrm{U}}(\mathbf{U}^{n+1}, \mathbf{G}^{n+1}) = \frac{\rho_{\mathrm{f}}}{\Delta t} M_{\mathrm{ff}}^{\mathrm{f}}(\mathbf{V}_{\mathrm{f}}^{n+1} - \mathbf{V}_{\mathrm{f}}^{n}) + \frac{\rho_{\mathrm{f}}}{\Delta t} M_{\mathrm{f}\Sigma}^{\mathrm{f}}(\mathbf{V}_{\Sigma}^{n+1} - \mathbf{V}_{\Sigma}^{n}) + C_{\mathrm{ff}}(\mathbf{V}^{n}, \mathbf{G}^{n+1}, \mathbf{G}^{n})\mathbf{V}_{\mathrm{f}}^{n+1} +$$
$$+ C_{\mathrm{f}\Sigma}(\mathbf{V}^{n}, \mathbf{G}^{n+1}, \mathbf{G}^{n})\mathbf{V}_{\Sigma}^{n+1} + K_{\mathrm{ff}}^{\mathrm{f}}\mathbf{U}_{\mathrm{f}}^{n+1} + K_{\mathrm{f}\Sigma}^{\mathrm{f}}\mathbf{U}_{\Sigma}^{n+1} + B_{\mathrm{f}}^{T}\mathbf{P}^{n+1} \, ,$$

while the second one is given by

$$\mathbb{F}_f^P(\mathbf{U}^{n+1}, \mathbf{U}^n, \mathbf{G}^{n+1}, \mathbf{G}^n) = B_f \mathbf{V}_f^{n+1} + B\Sigma \mathbf{V}_\Sigma^{n+1} \ .$$

In the above equations,

$$M_{kl}^f \in \mathbb{R}^{N_k^f \times N_l^f} \qquad (M_{kl}^f)_{i,j} = \int_{\Omega_f^t} \boldsymbol{\varphi}_{k,i}^f \cdot \boldsymbol{\varphi}_{l,j}^f \qquad i \in \{1, \dots, N_k^f\},\ j \in \{1, \dots, N_l^f\}, \qquad k,l \in \{f, \Sigma\}$$

are the fluid velocity mass matrix blocks corresponding to the different combinations of interior and interface basis functions. C_{ff} and $C_{f\Sigma}$ arise from the discretization of the advection term of the momentum equation, and are given by:

$$C_{kl} \in \mathbb{R}^{N_k^f \times N_l^f} \qquad (C_{kl}^f)_{i,j} = \int_{\Omega_f^t} (\mathbf{w} \cdot \nabla) \boldsymbol{\varphi}_{l,k}^f \cdot \boldsymbol{\varphi}_{k,i}^f \qquad i \in \{1, \dots, N_k^f\},\ j \in \{1, \dots, N_l^f\}, \quad k,l \in \{f, \Sigma\} \ ,$$

in which $\mathbf{w}$ is the advection velocity, computed from the discrete velocity and fluid domain displacement vectors through

$$\mathbf{w} = \sum_{i=1}^{N_f^f} \left(\mathbf{U}_{f,i}^n - \frac{\mathbf{G}_{f,i}^{n+1} - \mathbf{G}_{f,i}^n}{\Delta t} \right) \boldsymbol{\varphi}_{f,i}^f + \sum_{i=1}^{N_\Sigma^f} \left(\mathbf{U}_{\Sigma,i}^n - \frac{\mathbf{G}_{\Sigma,i}^{n+1} - \mathbf{G}_{\Sigma,i}^n}{\Delta t} \right) \boldsymbol{\varphi}_{\Sigma,i}^f \ .$$

Matrices K_{ff}^f and $K_{f\Sigma}^f$ are stiffness matrices for the fluid, defined by

$$K_{kl}^f \in \mathbb{R}^{N_k^f \times N_l^f} \qquad (K_{kl}^g)_{i,j} = \int_{\widehat{\Omega}_f} 2\mu\varepsilon(\boldsymbol{\varphi}_{l,j}^f) : \nabla \boldsymbol{\varphi}_{k,i}^f \qquad i \in \{1, \dots, N_k^f\},\ j \in \{1, \dots, N_l^f\}, \quad k,l \in \{f, \Sigma\} \ ,$$

and the matrices B_f and B_Σ are defined by

$$B_k \in \mathbb{R}^{N^P \times N_k^f} \qquad (B_k)_{i,j} = \int_{\Omega_f^t} \psi_i \nabla \cdot \boldsymbol{\varphi}_{k,j}^f \qquad i \in \{1, \dots, N^P\}, \quad j \in \{1, \dots, N_k^f\} \quad k \in \{f, \Sigma\} \ .$$

Terms arising from the SUPG stabilization are not reported here for the sake of brevity, but they are discussed e.g. in [28, 76, 93, 102]

A.4 Coupling conditions

The kinematic coupling operator $\mathbb{C}_k$ is defined as

$$\mathbb{C}_k(\mathbf{U}^{n+1}, \mathbf{D}^{n+1}) = M_{\Sigma\Sigma} \left(\mathbf{V}_\Sigma^{n+1} - \frac{\mathbf{D}_\Sigma^{n+1} - \mathbf{D}_\Sigma^n}{\Delta t} \right) \ .$$

We remark that in the implementation of DN scheme and of monolithic scheme, the continuity of velocity is applied essentially, i.e. we strongly impose the constraint that fluid and structure velocity interface degrees of freedom are equal. However, this formulation of the kinematic coupling operator is relevant when defining the interface conditions involved in partitioned schemes based on Robin conditions [13, 14].

Dynamic coupling is imposed in residual form [13], so that the dynamic coupling operator $\mathbb{C}_d$ reads

$$\mathbb{C}_d(\mathbf{D}^{n+1}, \mathbf{U}^{n+1}, \mathbf{G}^{n+1}) = \frac{\rho_s}{\Delta t} M_{\Sigma s}^s(\mathbf{D}_s^{n+1} - 2\mathbf{D}_s^n + \mathbf{D}_s^{n-1}) + \frac{\rho_s}{\Delta t} M_{\Sigma\Sigma}^s(\mathbf{D}_\Sigma^{n+1} - 2\mathbf{D}_\Sigma^n + \mathbf{D}_\Sigma^{n-1}) +$$
$$+ K_\Sigma^s(\mathbf{D}^{n+1}) + \frac{\rho_f}{\Delta t} M_{\Sigma f}^f(\mathbf{V}_f^{n+1} - \mathbf{V}_f^n) + \frac{\rho_f}{\Delta t} M_{\Sigma\Sigma}^f(\mathbf{V}_\Sigma^{n+1} - \mathbf{V}_\Sigma^n) + C_{\Sigma f}(\mathbf{V}^n, \mathbf{G}^{n+1}, \mathbf{G}^n)\mathbf{V}_f^{n+1} +$$
$$+ C_{\Sigma\Sigma}(\mathbf{V}^n, \mathbf{G}^{n+1}, \mathbf{G}^n)\mathbf{V}_\Sigma^{n+1} + K_{\Sigma f}^f \mathbf{U}_f^{n+1} + K_{\Sigma\Sigma}^f \mathbf{U}_\Sigma^{n+1} + B_\Sigma^T \mathbf{P}^{n+1} \ .$$

B Relaxation and convergence acceleration

The convergence properties of PE and PI schemes can be enhanced by using suitable relaxation or convergence acceleration schemes. We embed such schemes in the operator $\mathbb{R}_{(k+1)}(\widetilde{\mathbf{D}}_{(k+1)}^{n+1}, \mathbf{D}_{(k)}^{n+1}, \mathbf{D}_{(k-1)}^{n+1}, \dots)$ that, for a given guess $\widetilde{\mathbf{D}}_{(k+1)}^{n+1}$ for the structure displacement at next iteration and the structure displacements of previous iterations, computes $\mathbf{D}_{(k+1)}^{n+1}$. We consider three different relaxation operators.

B.1 Static relaxation (SR)

The relaxation operator is given by [13, 24, 60]

$$\mathbb{R}_{(k+1)}(\widetilde{\mathbf{D}}_{(k+1)}^{n+1}, \mathbf{D}_{(k)}^{n+1}, \mathbf{D}_{(k-1)}^{n+1}, \dots) = \lambda \widetilde{\mathbf{D}}_{(k+1)}^{n+1} + (1-\lambda)\mathbf{D}_{(k)}^{n+1} \qquad k = 0, 1, 2, \dots \,, \tag{13}$$

where $\lambda \in (0, 1]$ is a suitable parameter whose choice is critical to the convergence of the scheme; in particular, large values of λ typically lead to a fast convergence (when convergence occurs), but too large values of λ may cause the scheme to diverge [24].

B.2 Aitken acceleration (AitA)

The relaxation operator is defined as [13, 60, 66]

$$\mathbb{R}_{(k+1)}(\widetilde{\mathbf{D}}_{(k+1)}^{n+1}, \mathbf{D}_{(k)}^{n+1}, \mathbf{D}_{(k-1)}^{n+1}, \dots) = \lambda_{(k+1)} \widetilde{\mathbf{D}}_{(k+1)}^{n+1} + (1-\lambda_{(k+1)})\mathbf{D}_{(k)}^{n+1} \qquad k = 0, 1, 2, \dots \,, \tag{14}$$

with $\lambda_{(k+1)}$ computed as [60]

$$\lambda_{(k+1)} = \lambda_{(k)} \frac{\widetilde{\mathbf{D}}_k^{n+1} \cdot \left(\widetilde{\mathbf{D}}_{(k+1)}^{n+1} - \mathbf{D}_{(k)}^{n+1} - \widetilde{\mathbf{D}}_k^{n+1} + -\mathbf{D}_{(k-1)}^{n+1}\right)}{\left\|\widetilde{\mathbf{D}}_{(k+1)}^{n+1} - \mathbf{D}_{(k)}^{n+1} - \widetilde{\mathbf{D}}_k^{n+1} + -\mathbf{D}_{(k-1)}^{n+1}\right\|} \qquad k = 0, 1, 2, \dots \,,$$

for λ_0 given. This scheme typically improves the convergence with respect to static relaxation [60]. However, the choice of the initial relaxation parameter λ_0 is still problem dependent and needs to be manually tuned [60].

B.3 Anderson acceleration (AndA)

Anderson acceleration (AndA) [6, 33, 99], also known as Anderson mixing, can be interpreted as a multi-secant method [33] or as a nonlinear generalization of GMRES [99] and is based on computing the new iterate making use of the previous m ones, with m a suitable integer parameter. While generally used for self-consistent field iterations in the computation of electronic structures [33], it has been also been applied to domain decomposition [99] and multiphysics problems [21] and can be used to accelerate the convergence of FSI fixed-point schemes [64].

The procedure behind Anderson acceleration can be detailed as follows [99]. Consider the fixed-point iteration

$$x_{(k+1)} = g(x_k)$$

used to compute the solution of $x = g(x)$. Then, given $m \in \mathbb{N}$ and an initial guess x_0, Anderson acceleration of the sequence $x_{(k+1)}$ can be computed as follows:

1. set $m_{(k)} = \min\{m, k\}$;

2. set $F_{(k)} = \left[f_{k-m_{(k)}}, f_{k-m_{(k)}+1}, \dots, f_{(k)}\right]$, where $f_i = g(x_i) - x_i$;

3. find $\alpha^{(k)} = \left[\alpha_0^{(k)}, \alpha_1^{(k)}, \dots, \alpha_{m_{(k)}}^{(k)}\right]^T = \arg\min_{\alpha \in A} \left\|F_{(k)}\alpha\right\|$, with

$$A = \left\{\alpha = \left[\alpha_0, \alpha_1, \dots, \alpha_{m_{(k)}}\right]^T \text{ such that } \sum_{i=0}^{m_{(k)}} \alpha_i = 1\right\};$$

4. set $x_{(k+1)} = \sum_{i=0}^{m_{(k)}} \alpha_i^{(k)} g(x_{k-m_{(k)}+i})$.

Details on how to interpret the method, as well as alternative formulations, criteria for the choice of m and implementation details can be found in [99].

References

[1] CINECA GALILEO100 technical specifications. https://wiki.u-gov.it/confluence/display/SCAIUS/UG3.3%3A+GALILEO100+UserGuide.

[2] Official `deal.ii` website. https://www.dealii.org/.

[3] Official `life`$^\text{x}$ website. https://lifex.gitlab.io/lifex/.

[4] D. Ambrosi, G. Arioli, F. Nobile, and A. Quarteroni. Electromechanical coupling in cardiac dynamics: the active strain approach. *SIAM Journal on Applied Mathematics*, 71(2):605–621, 2011.

[5] D. Ambrosi and S. Pezzuto. Active stress vs. active strain in mechanobiology: constitutive issues. *Journal of Elasticity*, 107(2):199–212, 2012.

[6] D. G. Anderson. Iterative procedures for nonlinear integral equations. *Journal of the ACM*, 1965.

[7] D. Arndt, W. Bangerth, B. Blais, T. C. Clevenger, M. Fehling, A. V. Grayver, T. Heister, L. Heltai, M. Kronbichler, M. Maier, P. Munch, J. Pelteret, R. Rastak, I. Thomas, B. Turcksin, Z. Wang, and D. Wells. The `deal.II` library, version 9.2. *Journal of Numerical Mathematics*, 28(3):131–146, 2020.

[8] D. Arndt, W. Bangerth, D. Davydov, T. Heister, L. Heltai, M. Kronbichler, M. Maier, J. Pelteret, B. Turcksin, and D. Wells. The `deal.II` finite element library: design, features, and insights. *Computers & Mathematics with Applications*, 2020.

[9] M. Astorino, F. Chouly, and M. A. Fernández. Robin based semi-implicit coupling in fluid-structure interaction: Stability analysis and numerics. *SIAM Journal on Scientific Computing*, 31(6):4041–4065, 2010.

[10] M. Astorino, J. F. Gerbeau, O. Pantz, and K. F. Traoré. Fluid-structure interaction and multi-body contact. Application to the aortic valves. *Computer Methods in Applied Mechanics and Engineering*, 198:3603–3612, 2009.

[11] C. M. Augustin, A. Crozier, A. Neic, A. J. Prassl, E. Karabelas, T. Ferreira da Silva, J. F. Fernandes, F. Campos, T. Kuehne, and G. Plank. Patient-specific modeling of left ventricular electromechanics as a driver for haemodynamic analysis. *EP Europace*, 18(suppl_4):iv121–iv129, 2016.

[12] C. M. Augustin, A. Neic, M. Liebmann, A. J. Prassl, S. A. Niederer, G. Haase, and G. Plank. Anatomically accurate high resolution modeling of human whole heart electromechanics: a strongly scalable algebraic multigrid solver method for nonlinear deformation. *Journal of Computational Physics*, 305:622–646, 2016.

[13] S. Badia, F. Nobile, and C. Vergara. Fluid-structure partitioned procedures based on Robin transmission conditions. *Journal of Computational Physics*, 227:7021–7051, 2008.

[14] S. Badia, F. Nobile, and C. Vergara. Robin-Robin preconditioned Krylov methods for fluid-structure interaction problems. *Computer Methods in Applied Mechanics and Engineering*, 198:2768–2784, 2009.

[15] S. Badia, A. Quaini, and A. Quarteroni. Splitting methods based on algebraic factorization for fluid-structure interaction. *SIAM Journal on Scientific Computing*, 30(4):1778–1805, 2008.

[16] J. W. Banks, W. D. Henshaw, and D. W. Schwendeman. An analysis of a new stable partitioned algorithm for FSI problems. Part I: Incompressible flow and elastic solids. *Journal of Computational Physics*, 269:108–137, 2014.

[17] Y. Bazilevs, V. M. Calo, T. J. Hughes, and Y. Zhang. Isogeometric fluid-structure interaction: theory, algorithms, and computations. *Computational Mechanics*, 43(1):3–37, 2008.

[18] Y. Bazilevs, K. Takizawa, and T. E. Tezduyar. *Computational fluid-structure interaction: methods and applications*. John Wiley & Sons, 2013.

[19] P. J. Blanco and R. A. Feijóo. A 3D-1D-0D computational model for the entire cardiovascular system. *Mecánica Computacional*, 29(59):5887–5911, 2010.

[20] D. Bluestein and S. Einav. Transition to turbulence in pulsatile flow through heart valves—a modified stability approach. *Journal of biomechanical engineering*, 116(4):477–487, 1994.

[21] J. W. Both, N. A. Barnafi, F. A. Radu, P. Zunino, and A. Quarteroni. Iterative splitting schemes for a soft material poromechanics model. *Computer Methods in Applied Mechanics and Engineering*, 388:114183, 2022.

[22] M. Bukač, S. Čanić, R. Glowinski, J. Tambača, and A. Quaini. Fluid–structure interaction in blood flow capturing non-zero longitudinal structure displacement. *Journal of Computational Physics*, 235:515–541, 2013.

[23] E. Burman and M. A. Fernández. Explicit strategies for incompressible fluid-structure interaction problems: Nitsche type mortaring versus Robin–Robin coupling. *International Journal for Numerical Methods in Engineering*, 97(10):739–758, 2014.

[24] P. Causin, J. F. Gerbeau, and F. Nobile. Added-mass effect in the design of partitioned algorithms for fluid-structure interaction. *Computer Methods in Applied Mechanics and Engineering*, 194:4506–4527, 2005.

[25] Y. Cheng, H. Oertel, and T. Schenkel. Fluid-structure coupled cfd simulation of the left ventricular flow during filling phase. *Annals of biomedical engineering*, 33(5):567–576, 2005.

[26] P. Crosetto, S. Deparis, G. Fourestey, and A. Quarteroni. Parallel algorithms for fluid-structure interaction problems in haemodynamics. *SIAM Journal on Scientific Computing*, 33(4):1598–1622, 2011.

[27] Y. Dabiri, J. Yao, K. L. Sack, G. S. Kassab, and J. M. Guccione. Tricuspid valve regurgitation decreases after mitraclip implantation: Fluid structure interaction simulation. *Mechanics research communications*, 97:96–100, 2019.

[28] L. Dede', F. Menghini, and A. Quarteroni. Computational fluid dynamics of blood flow in an idealized left human heart. *International Journal for Numerical Methods in Biomedical Engineering*, 2019.

[29] S. Deparis, M. Discacciati, G. Fourestey, and A. Quarteroni. Fluid-structure algorithms based on Steklov-Poincarè operators. *Computer Methods in Applied Mechanics and Engineering*, 195(41–43):5797–5818, 2006.

[30] S. Deparis, D. Forti, G. Grandperrin, and A. Quarteroni. FaCSI: A block parallel preconditioner for fluid–structure interaction in hemodynamics. *Journal of Computational Physics*, 327:700–718, 2016.

[31] S. Deparis, G. Grandperrin, and A. Quarteroni. Parallel preconditioners for the unsteady Navier–Stokes equations and applications to hemodynamics simulations. *Computers & Fluids*, 92:253–273, 2014.

[32] D. R. Einstein, F. Del Pin, X. Jiao, A. P. Kuprat, J. P. Carson, K. S. Kunzelman, R. P. Cochran, J. M. Guccione, and M. B. Ratcliffe. Fluid–structure interactions of the mitral valve and left heart: comprehensive strategies, past, present and future. *International Journal for Numerical Methods in Biomedical Engineering*, 26(3-4):348–380, 2010.

[33] H. R. Fang and Y. Saad. Two classes of multisecant methods for nonlinear acceleration. *Numerical Linear Algebra with Applications*, 16:197–221, 2009.

[34] M. Fernández, J. F. Gerbeau, and C. Grandmont. A projection semi-implicit scheme for the coupling of an elastic structure with an incompressible fluid. *International Journal for Numerical Methods in Engineering*, 69:794–821, 2007.

[35] M. Fernández and M. Moubachir. A Newton method using exact jacobians for solving fluid-structure coupling. *Computers and Structures*, 83(2-3):127–142, 2005.

[36] M. A. Fernández, J. Mullaert, and M. Vidrascu. Explicit Robin–Neumann schemes for the coupling of incompressible fluids with thin-walled structures. *Computer Methods in Applied Mechanics and Engineering*, 267:566–593, 2013.

[37] I. Fumagalli, M. Fedele, C. Vergara, L. Dede', S. Ippolito, F. Nicolò, C. Antona, R. Scrofani, and A. Quarteroni. An image-based computational hemodynamics study of the Systolic Anterior Motion of the mitral valve. *Computers in Biology and Medicine*, 123(May):103922, 2020.

[38] T. Gerach, S. Schuler, J. Fröhlich, L. Lindner, E. Kovacheva, R. Moss, E. M. Wülfers, G. Seemann, C. Wieners, and A. Loewe. Electro-mechanical whole-heart digital twins: A fully coupled multi-physics approach. *Mathematics*, 9(11):1247, 2021.

[39] L. Gerardo-Giorda, F. Nobile, and C. Vergara. Analysis and optimization of Robin-Robin partitioned procedures in fluid-structure interaction problems. *SIAM Journal on Numerical Analysis*, 48(6):2091–2116, 2010.

[40] A. Gerbi. *Numerical approximation of cardiac electro-fluid-mechanical models: coupling strategies for large-scale simulation.* PhD thesis, EPFL, 2018.

[41] A. Gerbi, L. Dede', and A. Quarteroni. A monolithic algorithm for the simulation of cardiac electromechanics in the human left ventricle. *Mathematics in Engineering*, 1(1):1–37, 2018.

[42] G. Gigante, G. Sambataro, and C. Vergara. Optimized Schwarz methods for spherical interfaces with application to fluid-structure interaction. *SIAM Journal on Scientific Computing*, 42(2):A751–A770, 2020.

[43] G. Gigante and C. Vergara. Analysis and optimization of the generalized Schwarz method for elliptic problems with application to fluid–structure interaction. *Numerische Mathematik*, 131(2):369–404, 2015.

[44] G. Gigante and C. Vergara. On the choice of interface parameters in Robin–Robin loosely coupled schemes for fluid–structure interaction. *Fluids*, 6(6):213, 2021.

[45] G. Gigante and C. Vergara. On the stability of a loosely-coupled scheme based on a Robin interface condition for fluid-structure interaction. *Computers & Mathematics with Applications*, 96:109–119, 2021.

[46] J. M. Guccione and A. D. McCulloch. Finite element modeling of ventricular mechanics. In L. Glass, P. Hunter, and A. D. McCulloch, editors, *Theory of Heart*. Springer, 1991.

[47] G. Guidoboni, R. Glowinski, N. Cavallini, and S. Canic. Stable loosely-coupled-type algorithm for fluid–structure interaction in blood flow. *Journal of Computational Physics*, 228(18):6916–6937, 2009.

[48] V. Gurev, T. Lee, J. Constantino, H. Arevalo, and N. A. Trayanova. Models of cardiac electromechanics based on individual hearts imaging data: Image-based electromechanical models of the heart. *Biomechanics and Modeling in Mechanobiology*, 10(3):295–306, 2011.

[49] W. Hackbush. *Multigrid methods and applications*. Springer Verlag, 1985.

[50] M. Hirschhorn, V. Tchantchaleishvili, R. Stevens, J. Rossano, and A. Throckmorton. Fluid–structure interaction modeling in cardiovascular medicine–a systematic review 2017–2019. *Medical engineering & physics*, 78:1–13, 2020.

[51] M. Hirschvogel, M. Bassilious, L. Jagschies, S. M. Wildhirt, and M. W. Gee. A monolithic 3D-0D coupled closed-loop model of the heart and the vascular system: experiment-based parameter estimation for patient-specific cardiac mechanics. *International journal for numerical methods in biomedical engineering*, 33(8):e2842, 2017.

[52] G. A. Holzapfel and R. W. Ogden. Constitutive modelling of passive myocardium: A structurally based framework for material characterization. *Philosophical Transactions of the Royal Society A: Mathematical, Physical and Engineering Sciences*, 367(1902):3445–3475, 2009.

[53] M. C. Hsu, D. Kamensky, Y. Bazilevs, M. S. Sacks, and T. J. R. Hughes. Fluid–structure interaction analysis of bioprosthetic heart valves: significance of arterial wall deformation. *Computational mechanics*, 54(4):1055–1071, 2014.

[54] T. J. R. Hughes. *The Finite Element Method*. Prentice-Hall, 2000.

[55] T. J. R. Hughes, W. K. Liu, and T. K. Zimmerman. Lagrangian-Eulerian finite element formulation for incompressible viscous flows. *Computer Methods in Applied Mechanics and Engineering*, 29(3):329–349, 1981.

[56] E. Karabelas, M. A. F. Gsell, C. M. Augustin, L. Marx, A. Neic, A. J. Prassl, L. Goubergrits, T. Kuehne, and G. Plank. Towards a computational framework for modeling the impact of aortic coarctations upon left ventricular load. *Frontiers in physiology*, 9:538, 2018.

[57] A. Katz. *Physiology of the Heart*. M - Medicine Series. Wolters Kluwer Health/Lippincott Williams & Wilkins Health, 2010.

[58] R. C. P. Kerckhoffs, M. L. Neal, Q. Gu, J. B. Bassingthwaighte, J. H. Omens, and A. D. McCulloch. Coupling of a 3d finite element model of cardiac ventricular mechanics to lumped systems models of the systemic and pulmonic circulation. *Annals of biomedical engineering*, 35(1):1–18, 2007.

[59] U. Küttler, M. Gee, C. Förster, A. Comerford, and W. A. Wall. Coupling strategies for biomedical fluid-structure interaction problems. *International Journal for Numerical Methods in Biomedical Engineering*, 26(3-4):305–321, 2010.

[60] U. Küttler and W. A. Wall. Fixed-point fluid-structure interaction solvers with dynamic relaxation. *Computational Mechanics*, 43(1):61–72, 2008.

[61] M. Landajuela, M. Vidrascu, D. Chapelle, and M. A. Fernández. Coupling schemes for the FSI forward prediction challenge: Comparative study and validation. *International Journal for Numerical Methods in Biomedical Engineering*, 33(4):2813, 2017.

[62] J. Liu and A. L. Marsden. A unified continuum and variational multiscale formulation for fluids, solids, and fluid–structure interaction. *Computer methods in applied mechanics and engineering*, 337:549–597, 2018.

[63] G. Luraghi, W. Wu, F. De Gaetano, J. F. R. Matas, G. D. Moggridge, M. Serrani, J. Stasiak, M. L. Costantino, and F. Migliavacca. Evaluation of an aortic valve prosthesis: Fluid-structure interaction or structural simulation? *Journal of biomechanics*, 58:45–51, 2017.

[64] M. Mehl, B. Uekermann, H. Bijl, D. Blom, B. Gatzhammer, and A. Van Zuijlen. Parallel coupling numerics for partitioned fluid–structure interaction simulations. *Computers & Mathematics with Applications*, 71(4):869–891, 2016.

[65] V. Meschini, R. Mittal, and R. Verzicco. Systolic anterior motion in hypertrophic cardiomyopathy: a fluid–structure interaction computational model. *Theoretical and Computational Fluid Dynamics*, 35(3):381–396, 2021.

[66] D. P. Mok, W. A. Wall, and E. Ramm. Accelerated iterative substructuring schemes for instationary fluid-structure interaction. *Computational Fluid and Solid Mechanics*, 2:1325–1328, 2001.

[67] C. M. Murea and S. Sy. A fast method for solving fluid–structure interaction problems numerically. *International journal for numerical methods in fluids*, 60(10):1149–1172, 2009.

[68] F. Nobile, M. Pozzoli, and C. Vergara. Time accurate partitioned algorithms for the solution of fluid-structure interaction problems in haemodynamics. *Compupters & Fluids*, 86:470–482, 2013.

[69] F. Nobile, M. Pozzoli, and C. Vergara. Inexact accurate partitioned algorithms for fluid–structure interaction problems with finite elasticity in haemodynamics. *Journal of Computational Physics*, 273:598–617, 2014.

[70] D. Nordsletten. *Fluid-solid coupling for the simulation of left ventricular dynamics*. PhD thesis, University of Oxford, 2009.

[71] D. Nordsletten, M. McCormick, P. J. Kilner, P. Hunter, D. Kay, and N. P. Smith. Fluid-solid coupling for the investigation of diastolic and systolic human left ventricular function. *International Journal for Numerical Methods in Biomedical Engineering*, 27:1017–1039, 2011.

[72] R. W. Ogden. *Non-linear Elastic Deformations*. Courier Corporation, 1997.

[73] M. R. Pfaller, J. M. Hörmann, M. Weigl, A. Nagler, R. Chabiniok, C. Bertoglio, and W. A. Wall. The importance of the pericardium for cardiac biomechanics: from physiology to computational modeling. *Biomechanics and modeling in mechanobiology*, 18(2):503–529, 2019.

[74] R. Piersanti, P. C. Africa, M. Fedele, C. Vergara, L. Dede', A. F. Corno, and A. Quarteroni. Modeling cardiac muscle fibers in ventricular and atrial electrophysiology simulations. *Computer Methods in Applied Mechanics and Engineering*, 373:113468, 2021.

[75] A. Quaini and A. Quarteroni. A semi-implicit approach for fluid-structure interaction based on an algebraic fractional step. *Mathematicals Models and Methods in Applied Sciences*, 17:957–983, 2007.

[76] A. Quarteroni. *Numerical Models for Differential Problems.* Springer, 2017.

[77] A. Quarteroni, L. Dede', A. Manzoni, and C. Vergara. *Mathematical Modelling of the Human Cardiovascular System-Data, Numerical Approximation, Clinical Applications.* Cambridge University Press, 2019.

[78] A. Quarteroni, T. Lassila, S. Rossi, and R. Ruiz-Baier. Integrated Heart—Coupling multiscale and multiphysics models for the simulation of the cardiac function. *Computer Methods in Applied Mechanics and Engineering*, 314:345–407, 2017.

[79] A. Quarteroni, A. Veneziani, and C. Vergara. Geometric multiscale modeling of the cardiovascular system, between theory and practice. *Computer Methods in Applied Mechanics and Engineering*, 302:193–252, 2016.

[80] F. Regazzoni, L. Dede', and A. Quarteroni. Biophysically detailed mathematical models of multiscale cardiac active mechanics. *PLOS Computational Biology*, 16(10):1–42, 10 2020.

[81] F. Regazzoni, L. Dede', and A. Quarteroni. Machine learning of multiscale active force generation models for the efficient simulation of cardiac electromechanics. *Computer Methods in Applied Mechanics and Engineering*, 370:113628, 10 2020.

[82] F. Regazzoni, M. Salvador, P. C. Africa, M. Fedele, L. Dede', and A. Quarteroni. A cardiac electromechanics model coupled with a lumped parameters model for closed-loop blood circulation. Part I: model derivation. *arXiv preprint arXiv:2011.15040*, 2020.

[83] F. Regazzoni, M. Salvador, P. C. Africa, M. Fedele, L. Dede', and A. Quarteroni. A cardiac electromechanics model coupled with a lumped parameters model for closed-loop blood circulation. Part II: numerical approximation. *arXiv preprint arXiv:2011.15051*, 2020.

[84] S. Rossi, T. Lassila, R. Ruiz-Baier, A. Sequeira, and A. Quarteroni. Thermodynamically consistent orthotropic activation model capturing ventricular systolic wall thickening in cardiac electromechanics. *European Journal of Mechanics A/Solids*, 48:129–142, 2014.

[85] M. Salvador, M. Fedele, P. C. Africa, E. Sung, A. Prakosa, J. Chrispin, N. Trayanova, and A. Quarteroni. Electromechanical modeling of human ventricles with ischemic cardiomyopathy: numerical simulations in sinus rhythm and under arrhythmia. *Computers in Biology and Medicine*, 136:104674, 2021.

[86] M. Salvador, F. Regazzoni, S. Pagani, L. Dede, N. Trayanova, and A. Quarteroni. The role of mechano-electric feedbacks and hemodynamic coupling in scar-related ventricular tachycardia. *arXiv preprint arXiv:2110.15401*, 2021.

[87] A. Santiago, J. Aguado-Sierra, M. Zavala-Aké, R. Doste-Beltran, S. Gòmez, R. Arìs, J. C. Cajas, and E. Casoni. Fully coupled fluid-electro-mechanical model of the human heart for supercomputers. *International Journal for Numerical Methods in Biomedical Engineering*, 34:e3140, 2018.

[88] K. Stein, T. Tezduyar, and R. Benney. Mesh moving techniques for fluid-structure interactions with large displacements. *Journal of Applied Mechanics, Transactions ASME*, 70(1):58–63, 2003.

[89] M. Strocchi, M. A. Gsell, C. M. Augustin, O. Razeghi, C. H. Roney, A. J. Prassl, E. J. Vigmond, J. M. Behar, J. S. Gould, C. A. Rinaldi, M. J. Bishop, G. Plank, and S. A. Niederer. Simulating ventricular systolic motion in a four-chamber heart model with spatially varying robin boundary conditions to model the effect of the pericardium. *Journal of Biomechanics*, 101:109645, 2020.

[90] S. Sugiura, T. Washio, A. Hatano, J. Okada, H. Watanabe, and T. Hisada. Multi-scale simulations of cardiac electrophysiology and mechanics using the university of tokyo heart simulator. *Progress in biophysics and molecular biology*, 110(2-3):380–389, 2012.

[91] A. Tagliabue, L. Dede', and A. Quarteroni. Complex blood flow patterns in an idealized left ventricle: A numerical study. *Chaos*, 27(9):093939, 2017.

[92] T. Terahara, K. Takizawa, T. E. Tezduyar, Y. Bazilevs, and M. C. Hsu. Heart valve isogeometric sequentially-coupled fsi analysis with the space–time topology change method. *Computational Mechanics*, pages 1–21, 2020.

[93] T. Tezduyar and S. Sathe. Stabilization parameters in supg and pspg formulations. *Journal of computational and applied mechanics*, 4(1):71–88, 2003.

[94] A. This, L. Boilevin-Kayl, M. A. Fernández, and J. F. Gerbeau. Augmented resistive immersed surfaces valve model for the simulation of cardiac hemodynamics with isovolumetric phases. *International Journal for Numerical Methods in Biomedical Engineering*, 36(3):1–26, 2020.

[95] T. Usyk, I. LeGrice, and A. D. McCulloch. Computational model of three-dimensional cardiac electromechanics. *Computing and Visualization in Science*, 4:249–257, 2002.

[96] A. C. Verkaik, A. C. B. Bogaerds, F. Storti, and F. N. Van De Vosse. A coupled overlapping domain method for the computation of transitional flow through artificial heart valves. In *ASME 2012 Summer Bioengineering Conference (SBC 2012)*, pages 217–218. American Society of Mechanical Engineers, 2012.

[97] I. E. Vignon-Clementel, C. A. Figueroa, K. E. Jansen, and C. A. Taylor. Outflow boundary conditions for 3D simulations of non-periodic blood flow and pressure fields in deformable arteries. *Computer methods in biomechanics and biomedical engineering*, 13(5):625–640, 2010.

[98] F. Viola, V. Meschini, and R. Verzicco. Fluid–Structure-Electrophysiology interaction (FSEI) in the left-heart: A multi-way coupled computational model. *European Journal of Mechanics, B/Fluids*, 79:212–232, 2020.

[99] H. F. Walker and P. Ni. Anderson acceleration for fixed-point iterations. *SIAM Journal on Numerical Analysis*, 49:1715–1735, 2011.

[100] H. Watanabe, S. Sugiura, H. Kafuku, and T. Hisada. Multiphysics simulation of left ventricular filling dynamics using fluid-structure interaction finite element method. *Biophysical journal*, 87(3):2074–2085, 2004.

[101] Q. Zhang and T. Hisada. Analysis of fluid-structure interaction problems with structural buckling and large domain changes by ale finite element method. *Computer Methods in Applied Mechanics and Engineering*, 190:6341–6357, 2001.

[102] A. Zingaro, L. Dede', F. Menghini, and A. Quarteroni. Hemodynamics of the heart's left atrium based on a Variational Multiscale-LES numerical method. *European Journal of Mechanics-B/Fluids*, 89:380–400, 2021.

[103] A. Zingaro, I. Fumagalli, L. Dede', M. Fedele, P. C. Africa, A. F. Corno, and A. Quarteroni. A multiscale CFD model of blood flow in the human left heart coupled with a lumped parameter model of the cardiovascular system. *MOX Report*, 56, 2021.

MOX Technical Reports, last issues

Dipartimento di Matematica
Politecnico di Milano, Via Bonardi 9 - 20133 Milano (Italy)

76/2021 Ponti, L.; Perotto, S.; Sangalli, L.M.
A PDE-regularized smoothing method for space-time data over manifolds with application to medical data

77/2021 Guo, M.; Manzoni, A.; Amendt, M.; Conti, P.; Hesthaven, J.S.
Multi-fidelity regression using artificial neural networks: efficient approximation of parameter-dependent output quantities

73/2021 Marcinno, F.; Zingaro, A.; Fumagalli, I.; Dede', L.; Vergara, C.
A computational study of blood flow dynamics in the pulmonary arteries

75/2021 Cicci, L.; Fresca, S.; Pagani, S.; Manzoni, A.; Quarteroni, A.
Projection-based reduced order models for parameterized nonlinear time-dependent problems arising in cardiac mechanics

74/2021 Orlando,G.; Barbante, P. F.; Bonaventura, L.
An efficient IMEX-DG solver for the compressible Navier-Stokes equations with a general equation of state

71/2021 Franco, N.; Manzoni, A.; Zunino, P.
A Deep Learning approach to Reduced Order Modelling of parameter dependent Partial Differential Equations

72/2021 Fresca, S.; Manzoni, A.
POD-DL-ROM: enhancing deep learning-based reduced order models for nonlinear parametrized PDEs by proper orthogonal decomposition

70/2021 Beirao da Veiga, L.; Canuto, C.; Nochetto, R.H.; Vacca, G.; Verani, M.
Adaptive VEM: Stabilization-Free A Posteriori Error Analysis

69/2021 Antonietti, P.F.; Caldana, M.; Dede', L.
Accelerating Algebraic Multigrid Methods via Artificial Neural Networks

68/2021 Regazzoni, F.; Salvador, M.; Dede', L.; Quarteroni, A.
A machine learning method for real-time numerical simulations of cardiac electromechanics